iScience

CellPress
OPEN ACCESS

Article

DNA repair and cholesterol-mediated drug efflux induce dose-dependent chemoresistance in nutrient-deprived neuroblastoma cells

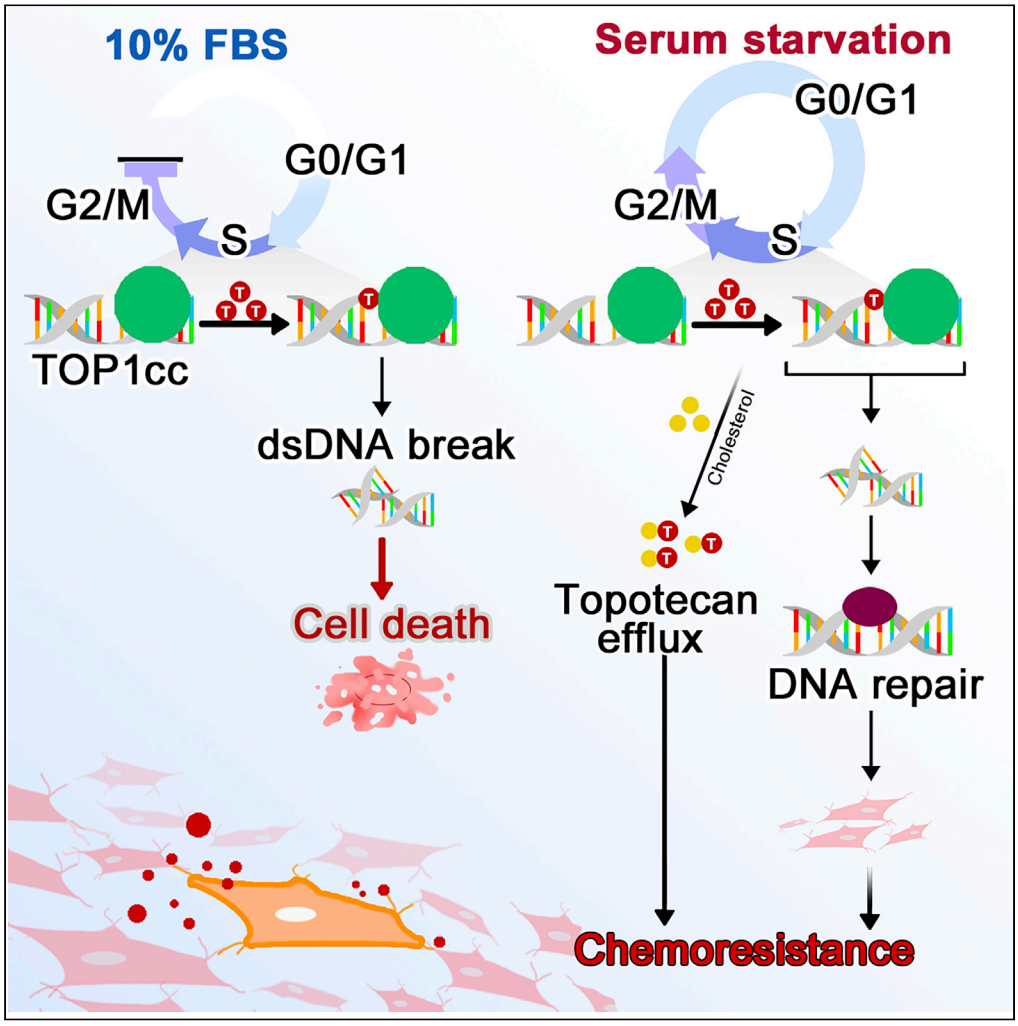

Soo Yeon Chae, Dowoon Nam, Do Young Hyeon, ..., Daehee Hwang, Sang-Won Lee, Hugh I. Kim

daehee@snu.ac.kr (D.H.)
sw_lee@korea.ac.kr (S.-W.L.)
hughkim@korea.ac.kr (H.I.K.)

Highlights

The survival rate was increased on nutrient-deprived human neuroblastoma cells

Performed proteomics and network analysis-based pharmacodynamic study

DNA repair was accelerated resistance in nutrient-deprived human neuroblastoma cells

Cholesterol-mediated efflux was increased at resistance conditions

Chae et al., iScience 24, 102325
April 23, 2021
https://doi.org/10.1016/j.isci.2021.102325

iScience

CellPress
OPEN ACCESS

Article

DNA repair and cholesterol-mediated drug efflux induce dose-dependent chemoresistance in nutrient-deprived neuroblastoma cells

Soo Yeon Chae,[1,2,5] Dowoon Nam,[1,2,5] Do Young Hyeon,[3,5] Areum Hong,[1,5] Timothy Dain Lee,[3] Sujin Kim,[1,2] Dongjoon Im,[1,2] Jiwon Hong,[1,2] Chaewon Kang,[1,2] Ji Won Lee,[4] Daehee Hwang,[3,*] Sang-Won Lee,[1,2,*] and Hugh I. Kim[1,2,6,*]

SUMMARY

Neuroblastoma is a solid, heterogeneous pediatric tumor. Chemotherapy is widely used to treat neuroblastoma. However, dose-dependent responses and chemoresistance mechanisms of neuroblastoma cells to anticancer drugs remain challenging. Here, we investigated the dose-dependent effects of topotecan on human neuroblastoma cells (SK-N-SH, SH-SY5Y, and SK-N-BE) under various nutrient supply conditions. Serum-starved human neuroblastoma cells showed reduced toxicity. Their survival rate increased upon treatment with a high concentration (1 μM) of topotecan. Quantitative profiling of global and phosphoproteome identified 12,959 proteins and 48,812 phosphosites, respectively, from SK-N-SH cells. Network analysis revealed that topotecan upregulated DNA repair and cholesterol-mediated topotecan efflux, resulting in topotecan resistance. Results of DNA damage assay, cell cycle, and quantitative analyses of membrane cholesterol supported the validity of these resistance factors and their applicability to all neuroblastoma cells. Our results provide a model for high dose-dependent chemoresistance in neuroblastoma cells that could enable a patient-dependent chemotherapy screening strategy.

INTRODUCTION

Neuroblastoma is the most common extracranial solid pediatric tumor, accounting for 6-10% of all childhood cancers. Neuroblastoma tumors originate from precursor cells in the sympathetic nervous system or the adrenal medulla (Maris et al., 2007; Stiller and Parkin, 1992; Maris and Matthay, 1999; Johnsen et al., 2018, 2019). The disease course of neuroblastoma is highly heterogeneous, and factors such as the age at diagnosis, stage, and tumor biology are known to affect treatment outcomes (Cheung and Dyer, 2013; Maris, 2010; Coldman et al., 1980). The current treatment strategy for neuroblastoma is tailored according to the risk stratification based on clinical and biological factors (Cohn et al., 2009; Leclair et al., 2004). Multicenter clinical trials offer tailored treatment approaches that have significantly improved the outcomes for neuroblastoma over the past decades, particularly for patients with low- and intermediate-risk neuroblastoma (Van Arendonk and Chung, 2019; Mossé et al., 2014). The treatment outcome for high-risk neuroblastoma has also been improved with intensive multimodal treatment. However, a substantial number of patients still experience relapse or progression (Herd et al., 2019; Morgenstern et al., 2013).

Anticancer drugs often fail to treat neuroblastoma due to the respective differences in the phenotypic profiles of tumors (Maeda and Khatami, 2018; Ngan, 2015; Hiyama and Hiyama, 2005). To optimize therapeutic outcomes given the individual differences, drug stability and efficacy tests using human cells in the form of 2-dimensional (2D) cell cultures or xenografts are commonly performed prior to the treatment (Niu and Wang, 2015; Macaire et al., 2019; Zanoni et al., 2016). However, drug responses in patients differ from those observed in cellular model systems. Under *in vivo* conditions, solid tumors are multicellular spheroid structures, the interiors of which are divided into three layers: the proliferating zone, the quiescent viable cell zone, and the necrotic core (Edmondson et al., 2014; Kim, 2005; Khaitan et al., 2006). Cells in the deeper regions of a tumor are deprived of oxygen, nutrients, and growth factors (Minchinton and Tannock, 2006; Höckel and Vaupel, 2001). Cells grown in 2D cultures under serum starvation show the morphology

[1]Department of Chemistry, Korea University, Seoul 02841, Republic of Korea

[2]Center for Proteogenome Research, Korea University, Seoul 02841, Republic of Korea

[3]Department of Biological Sciences, Seoul National University, Seoul 08826, Republic of Korea

[4]Department of Pediatrics, Samsung Medical Center, Sungkyunkwan University School of Medicine, Seoul 06351, Republic of Korea

[5]These authors contributed equally

[6]Lead contact

*Correspondence: daehee@snu.ac.kr (D.H.), sw_lee@korea.ac.kr (S.-W.L.), hughkim@korea.ac.kr (H.I.K.)

https://doi.org/10.1016/j.isci.2021.102325

and behavior similar to those shown by cells in the interior of tumors due to an analogous environment characterized by poor vascularization and nutrient-deprived condition (Levin et al., 2010). Therefore, a 2D culture of tumor cells under serum starvation serves as a good model system that mimics the interior of tumors; their study can provide information about the behavior of tumor cells at the molecular level.

Despite the heterogeneity in the phenotypic profiles of patients with neuroblastoma, equivalent doses of anticancer drugs are typically used in the chemotherapy regimen of individual patients. Despite extensive investigations into the molecular mechanisms of drug resistance (Longley and Johnston, 2005; Gottesman, 2002; Holohan et al., 2013) and the action of anticancer drugs (Starobova and Vetter, 2017; Alcindor and Beauger, 2011; Gregg et al., 1992), the dose-dependent effects of these drugs on tumor suppression have not been fully elucidated. Therefore, to develop therapeutic strategies for neuroblastoma, it is necessary to consider the concentration-dependent effects of anticancer drugs on tumor suppression.

Topotecan is an effective chemotherapeutic drug for induction therapy of high-risk neuroblastoma (De Ioris et al., 2011; Park et al., 2006). In this study, we investigated the dose-dependent effects of topotecan on human neuroblastoma cells (SK-N-SH, SH-SY5Y, and SK-N-BE). Serum-starved neuroblastoma cells commonly exhibited higher survival rates. Specifically, serum-starved SK-N-SH cells showed unique resistance to topotecan, when a high concentration (1 μM) of topotecan was used. We performed quantitative proteomic analysis of serum-starved SK-N-SH cells treated with topotecan to identify resistance factors. Functional enrichment and network analyses of the upregulated proteins in the resistance condition revealed that increased DNA repair activity and topotecan efflux as resistance factors. Time-resolved topotecan measurements performed using multiple reaction monitoring mass spectrometry (MRM-MS) further confirmed the decrease in topotecan levels in serum-starved SK-N-SH cells via the increased topotecan efflux. DNA damage assay, cell cycle analysis, and cholesterol detection confirmed the increased DNA repair activity and topotecan efflux in all neuroblastoma cells investigated in this study. Our results suggest a potential cellular mechanism for dose-dependent topotecan resistance and provide a strategy to predict topotecan efficacy in patients with neuroblastoma.

RESULTS

Nutrient-deprivation induces chemoresistance in human neuroblastoma cells

We first investigated the effects of topotecan on the survival of SK-N-SH, SH-SY5Y, and SK-N-BE cells under 10% fetal bovine serum (FBS) or serum starvation. The cells were treated with topotecan at concentrations ranging from 0.1 nM to 10 μM for up to 72 hr, and cell viability assays were performed every 24 hr after the initial drug treatment using cell counting kit-8 (CCK-8). Different cell viability trends were observed between 10% FBS and serum starvation conditions after 24 hr of the initial drug treatment (Figure 1). The viability of SK-N-SH, SH-SY5Y, and SK-N-BE human neuroblastoma cells was reduced significantly to 46.9, 42.6, and 50.5%, respectively, at 48 hr (Figure 1 and Table S1, Table depicting the viability of human neuroblastoma cells, related Figure 1) and 39.3, 36.7, and 52.0%, respectively, at 72 hr under 10% FBS after treatment with 1 μM topotecan (Table S1, Table depicting the viability of human neuroblastoma cells, related Figure 1 and Figure S1, dose-response viability curves at 72 hr, related Figure 1).

Serum-starved neuroblastoma cells exhibited higher overall survival rates than the cells grown in 10% FBS. For topotecan concentrations between 0.1 nM and 0.1 μM, topotecan-treated SK-N-SH, SH-SY5Y, and SK-N-BE cells showed a marginal increase in the viability under serum starvation compared to control cells not treated with topotecan (Figure 1). The findings suggest that topotecan treatment was not cytotoxic to the cells under serum starvation. However, when treated with 1 μM of topotecan, the viability of serum-starved SK-N-SH cells was significantly increased ($p < 0.01$) to approximately 1.6 folds (155%) with respect to control cells after 48 hr (Figure 1A and Table S1, Table depicting the viability of human neuroblastoma cells, related Figure 1) and 1.8 folds (179%) after 72 hr. A similar dose-dependent effect of topotecan was observed on the viability of SK-N-SH cells obtained from a different source (Korea Cell Line Bank) (Figure S2, Results of the cell viability assay performed with SK-N-SH cells obtained from a different source, related Figure 1). Although the effect was not as pronounced as that observed in SK-N-SH cells, the viability of serum-starved SH-SY5Y and SK-N-BE cells treated with 1 μM of topotecan was increased by 131% and 120%, respectively, after 72 hr (Table S1B and S1C, Table depicting the viability of human neuroblastoma cells, related Figures 1, Figure S1B, and S1C, dose-response viability curves at 72 hr, related Figure 1). These data indicate that neuroblastoma cells cultured in 10% FBS underwent apoptosis in response to topotecan treatment due to topotecan-induced DNA damage, whereas serum-starved cells might be resistant to apoptosis. Notably,

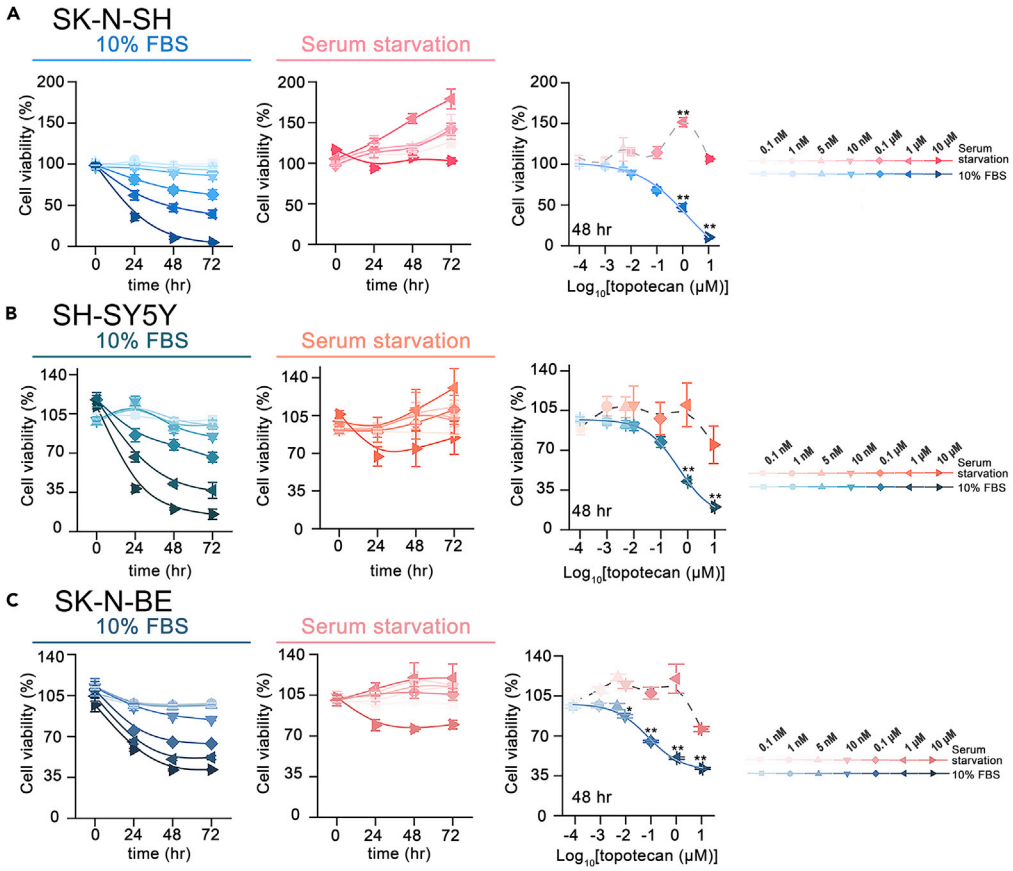

Figure 1. Cell viability assays of SK-N-SH, SH-SY5Y, and SK-N-BE human neuroblastoma cells treated with different concentrations of topotecan

Viability plots were constructed for cells incubated with 10% FBS (left) and for serum-starved cells (middle). Dose-response curves were also constructed at 48 hr under identical conditions. Data are presented as mean ± S.D. values derived from three independent experiments. *p < 0.05, **p < 0.01.

even when 10 μM of topotecan was administered, SK-N-SH, SH-SY5Y, and SK-N-BE cells exhibited significantly higher viability (102.8, 84.5, and 79.7%, respectively) under serum starvation after 72 hr than under 10% FBS (4.83, 15.5, and 41.6%, respectively). Collectively, these data indicate that serum starvation induces chemoresistance toward topotecan in neuroblastoma cells even up to high concentrations.

Quantitative proteomic profiling of SK-N-SH cells

To understand the molecular basis of the chemoresistance, we performed quantitative proteomic profiling of SK-N-SH cells. Proteins were extracted from the samples obtained after 5 min and 48 hr of 0.1 or 1 μM topotecan treatment or without topotecan treatment (control) under serum starvation or 10% FBS (Figures 2A and S3A, Proteomics experiments, related Figure 2). After tryptic digestion, the two sets of six peptide samples (control, 5 min, and 48 hr treatment under serum starvation or at 10% FBS) were labeled with 6-plex tandem mass tag (TMT) reagents (Figure S3, Proteomics experiments, related Figure 2). All 6-plex TMT-labeled peptide samples were pooled and the peptide pool was first subjected to immobilized metal affinity chromatography (IMAC) phosphopeptide enrichment as described previously (Park et al., 2015). The whole phosphopeptide sample was fractionated into 12 online non-contiguously fractionating and concatenating (NCFC) fractions using the dual-online-NCFC-reverse-phase/reverse-phase liquid chromatography (DO-NCFC-RP/RP-MS/MS) system (Lee et al., 2016) to generate 12 phosphopeptide LC-MS/MS data set. We obtained a total of 24 LC-MS/MS phospho data sets—12 after treatment with 0.1 μM topotecan and 12 after treatment with 1 μM topotecan (Figure S3, Proteomics experiments, related Figure 2). The flow-through sample (i.e. non-phosphopeptides) from the IMAC experiments was subsequently

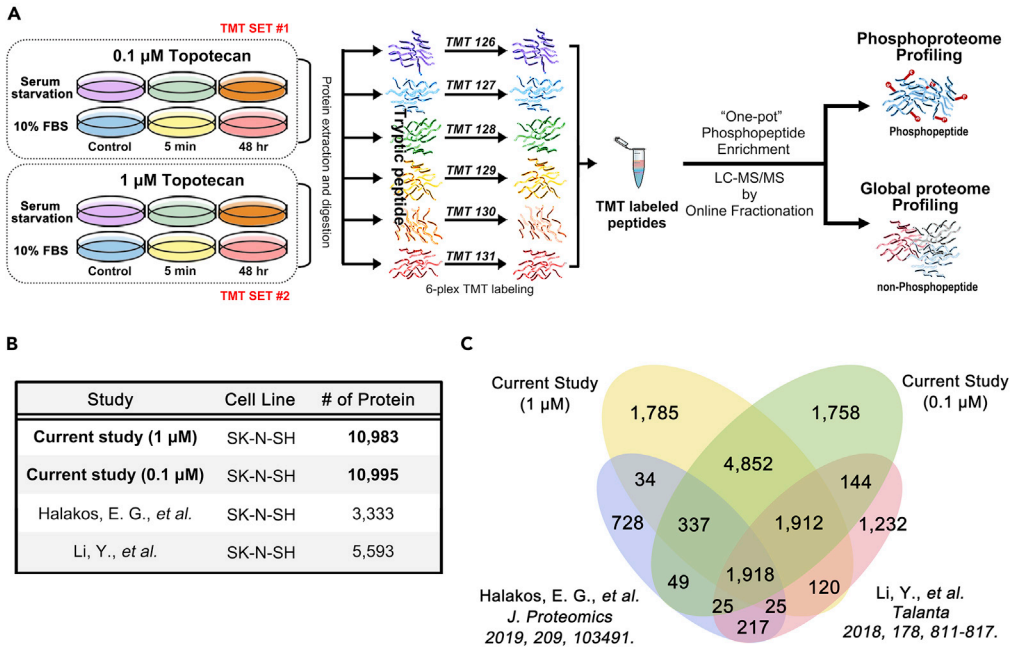

Study	Cell Line	# of Protein
Current study (1 μM)	SK-N-SH	**10,983**
Current study (0.1 μM)	SK-N-SH	**10,995**
Halakos, E. G., *et al.*	SK-N-SH	3,333
Li, Y., *et al.*	SK-N-SH	5,593

Figure 2. Global proteome and phosphoproteome profiling of SK-N-SH cells treated with 0.1 or 1 μM topotecan

(A) Schematic representation of the experimental procedure for quantitative proteomic analysis. Two sets (0.1 and 1 μM topotecan) of six cells (three cells of 10% FBS and three cells of serum starvation) were separately subjected to identical processes of protein extraction/digestion, 6-plex TMT-labeling, IMAC enrichment, and global/phosphoproteome analyses.

(B and C) The numbers of proteins characterized from SK-N-SH cells after treatment with 1 μM topotecan and 0.1 μM topotecan compared with the previously characterized proteome of the identical cell line.

fractionated into 24 online NCFC fractions using DO-NCFC-RP/RP-MS/MS system to generate 24 global LC-MS/MS data sets (Figure S3, Proteomics experiments, related Figure 2). For each of the 24 global LC-MS/MS data sets and the 12 phospho LC-MS/MS data sets, we identified the peptides through a search of the UniProt human reference database using the MS-GF + search engine using a target decoy setting and a peptide spectrum match-false discovery rate of 1%. From the SK-N-SH cells treated with 0.1 and 1 μM topotecan, we identified 285,027 and 281,156 non-redundant peptides, respectively, and 10,995 and 10,983 proteins with two or more sibling peptides, respectively (Figures 2B and 2C, and Data S1, The list of peptides and proteins from the proteomics analysis, related Figure 2). From the same peptide samples of 0.1 and 1 μM topotecan treatment, we identified 42,241 and 61,151 non-redundant phosphopeptides, respectively (Data S1, The list of peptides and proteins from the proteomics analysis, related Figure 2). There were high overlaps of the identified peptides and proteins between two TMT data sets (Figure S3B, Proteomics experiments, related Figure 2), supporting the validity of proteomic experiments. Compared to the previous proteome profile (3,333 proteins and 5,593 proteins from SK-N-SH cells) (Halakos et al., 2019; Li et al., 2018) and phosphoproteome profile (15,417 phosphopeptides from SK-N-BE2 cells) (Scaturro et al., 2018) obtained from neuroblastoma cells, our data represent a more comprehensive neuroblastoma proteome (Figures 2B and 2C) and phosphoproteome for the identification of protein signatures associated with topotecan resistance under serum starvation.

Topotecan resistance-associated protein signatures

Proteins whose abundance or phosphorylation was increased or decreased in serum-starved cells but not changed in those that were cultured with 10% FBS may contribute to topotecan resistance. To identify these proteins, we performed the following four comparisons of peptide abundances (TMT intensities) determined at 48 hr with and without treatment of 0.1 or 1 μM topotecan under 10% FBS or serum starvation: 0.1 μM vs. no treatment (0.1 μM FBS) and 1 μM vs. no treatment under 10% FBS (1 μM FBS), and 0.1 μM vs. no treatment (0.1 μM starvation) and 1 μM vs. no treatment (1 μM starvation) under serum starvation. From the four comparisons, we identified differentially expressed peptides and phosphopeptides with

absolute log_2-fold-changes > 1 (2-fold) and differentially expressed proteins (DEPs) with two or more unique differentially expressed peptides in the same direction (Data S2, The differentially expressed peptides and phosphopeptides and DEPs, related Figure 3.).

We then focused on the DEPs and differentially expressed phosphopeptides that were upregulated specifically under serum starvation but not changed under 10% FBS (Figures 3A and 3B, highlighted in red), which are likely to account for the induced property of topotecan resistance under serum starvation. To examine cellular processes associated with these upregulated proteins or the proteins containing the upregulated phosphopeptides, we performed enrichment analysis of gene ontology biological processes using the DAVID software (Huang et al., 2008). Upregulated proteins were mainly associated with processes related to the cell cycle (cell cycle, apoptotic process, and DNA damage response/DNA repair) and lipid synthesis/transport (Figure 3C). Upregulation of cell cycle proteins was consistent with the increased cell viability observed under serum starvation (Figure 1). Proteins with upregulated phosphorylation were mainly associated with the same cell-cycle-related processes that were enriched by the upregulated proteins, except for lipid synthesis/transport (Figure 3C). Instead, the insulin/mTOR signaling pathway, one of the most potent upstream signaling pathways of lipid synthesis/transport that activates sterol regulatory-element binding protein (SREBP) transcription factors, was enriched by these phosphoproteins. Since metabolic enzymes are commonly controlled by the protein abundance and rarely by phosphorylation, the complementary enrichment of lipid synthesis and insulin/mTOR signaling supports the validity of our global proteome and phosphoproteome.

To understand the collective effects of the upregulated proteins or phosphoproteins involved in the cell cycle, lipid synthesis/transport, and insulin/mTOR signaling on topotecan resistance, we built a network model (Figure 3D) describing the interactions among the upregulated proteins and phosphoproteins involved in these processes based on previously reported mode-of-action and topotecan resistance (Pommier, 2006; Liscovitch and Lavie, 2000). Topotecan binds to topoisomerase I (TOP1) in the TOP1 cleavage complex (TOP1cc), forming an irreversible TOP1cc that induces double-strand DNA (dsDNA) breaks during DNA replication at the S phase, followed by cell-cycle arrest at the G2 phase and apoptosis (Pommier, 2006; Kollmannsberger et al., 1999) (Figure 3D, top left). Topotecan induces dsDNA breaks and then activates the ATR-CHK1 pathway for their repair (Lambert et al., 2010; Adamson et al., 2012). Our network model revealed the downregulation of TOP1, upregulation of DNA repair proteins (BLM, ERCC1, and RRM2), and increased phosphorylation of proteins (CHK1, CDC25B, BLM, PARP4, and RRM2) in DNA repair signaling pathways under serum starvation (Figure 3D, left), which enhanced cell viability upon induction of DNA damage by topotecan. In addition, the network model showed the upregulation of proteins involved in cholesterol synthesis (HMGCS1, HMGCR, FDFT1, SQLE, CYP51A1, MSMO1, and DHCR24) and efflux (APOE) under serum starvation and increased topotecan efflux via topotecan chelation by cholesterol in a CAV1-dependent pathway (Liscovitch and Lavie, 2000) (Figure 3D, middle). The network model further showed the increased phosphorylation of proteins involved in the insulin/mTOR signaling (IRS1, PTPN1, PIK3R2, AKT2, AKT1S1, LPIN2, and EIF4EBP1), which led to the upregulation of cholesterol biosynthetic proteins via SREBP transcription factors (Figure 3D, right). These data collectively suggest that the upregulated DNA repair and cholesterol-mediated topotecan efflux and the activated insulin/mTOR signaling may contribute to the resistance to a high dose (1 μM) of topotecan in serum-starved SK-N-SH cells.

To check the validity of these findings obtained using the network analysis, we first performed immunoblotting (IB) to confirm the upregulation of the three representative proteins BLM, DHCR24, and Phospho-IRS-1 for increased DNA repair, cholesterol-mediated topotecan efflux, and insulin/mTOR signaling, respectively, in the network model. Western blotting assays confirmed the upregulation of BLM, DHCR24, and Phospho-IRS-1 proteins in SK-N-SH cells at 48 hr after 1 μM topotecan treatment under serum starvation; however, virtually no changes were observed under 10% FBS (Figure 3E). Taken together, these data support the contribution of increased DNA repair and cholesterol-mediated topotecan efflux to high-dose topotecan resistance in serum-starved SK-N-SH cells.

Increased DNA repair and altered cell cycle distribution associated with topotecan resistance under serum starvation

Chemotherapy-induced DNA-damage correlates with the release of the activated caspases (Rodríguez-Hernández et al., 2006). To verify improvements in DNA damage via enhanced DNA repair under serum starvation, as previously described (Koivusalo and Hietanen, 2004), we performed the DNA damage assay

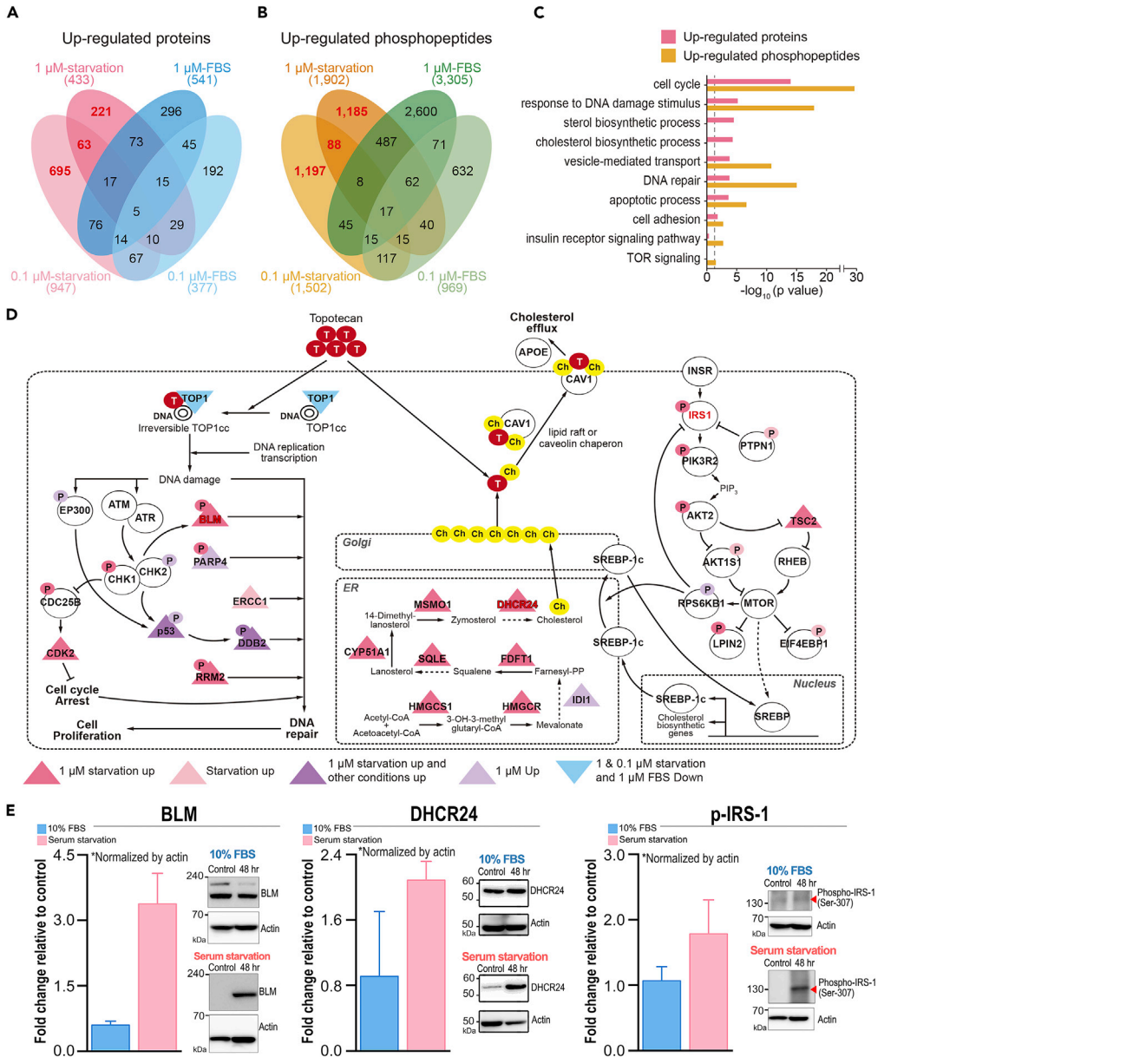

Figure 3. Protein signatures associated with topotecan resistance

(A and B) Venn diagram showing relationships between upregulated proteins (A) or phosphopeptides (B) under 0.1 μM and 1 μM starvation and 0.1 μM and 1 μM 10% FBS.

(C) Cellular processes enriched by the upregulated proteins or phosphopeptides specifically in serum-starved cells. The enrichment significance of each process is indicated as -$\log_{10}$ (p value), where the p value was computed using the DAVID software. The p value = 0.05 cutoff is indicated by a dotted line.

(D) Network model describing the cellular pathways of the proteins with increased/decreased abundances or phosphorylation in serum-starved cells. Circled P on a node indicates upregulated phosphorylation of the corresponding protein. Topotecan and cholesterol are denoted by "T" and "Ch," respectively. Conditions under which the abundance or phosphorylation of the corresponding protein is increased (up-pointing triangle) or decreased (down-pointing triangle) are indicated by the colors of nodes and circled P (see node legend). The names of proteins validated by the immunoblotting assay are shown in red. Solid arrows indicate direct activation, transport, and single-step conversion (e.g. conversion of metabolites in cholesterol biosynthesis pathway) of molecules, whereas dotted arrows indicate indirect activation and multi-step conversion of molecules. Solid inhibition symbols indicate direct inhibition of molecules.

(E) Quantification of the levels of BLM, DHCR24, and Phospho-IRS-1 (48 hr relative vs. control) by immunoblotting. The bar plots present mean ± S.D. values (n = 3).

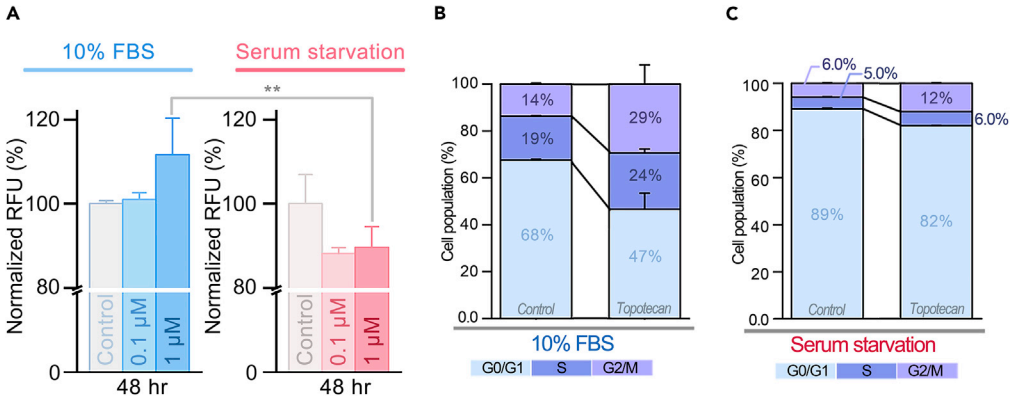

Figure 4. Bar-plot for the amount of activated caspase-3/7 in SK-N-SH cells and cell cycle analysis

(A) Bar-plot depicting the amount of activated caspase-3/7 in SK-N-SH cells and (B and C) cell cycle analysis. Plots were generated for cells incubated with 10% FBS and for serum-starved cells. Data are presented as mean ± S.D. values derived from three independent experiments. **p < 0.01.

by measuring the amounts of activated caspase-3/7 released into the culture media in the presence of 10% FBS and when exposed to serum starvation (48 hr after topotecan treatment). In the presence of 10% FBS, the amount of the activated caspase-3/7 released into the culture media by SK-N-SH cells slightly increased to 101% after treatment with 0.1 μM topotecan (Figure 4A). When treated with a higher concentration of topotecan, i.e., 1 μM, the amount further increased to approximately 112%. This increasing pattern was more evident at 72 hr after topotecan treatment (Figure S4, Bar-plot depicting the levels of activated caspase-3/7 at 72 h in SK-N-SH cells, related Figure 4). Such an increase in the levels of released activated caspase-3/7 confirmed the increase in DNA damage upon culturing the cells in presence of 10% FBS, consistent with the decreased viability in topotecan-treated SK-N-SH cells cultured with 10% FBS (Figure 1A). In contrast, serum-starved SK-N-SH cells exhibited significantly ($p < 0.01$) lower DNA damage than those cultured in the presence of 10% FBS, as indicated by the decreased amounts of activated caspase-3/7 48 hr after treatment with 0.1 μM (88.1%) and 1 μM (89.6%) topotecan (Figure 4A). These data confirm the increased DNA repair activity in serum-starved SK-N-SH cells, as indicated by the upregulation of BLM (Figure 3E).

Topotecan delays S phase progression during DNA replication by inducing dsDNA breaks and arrests the cells at the G2 phase. Our network model suggested a decrease in dsDNA breaks and an increase in the repair of dsDNA breaks, as indicated by the downregulation of TOP1 and upregulation of BLM, respectively. To examine the effects of decreased DNA damage and increased DNA repair on the cell cycle of serum-starved SK-N-SH cells, we next performed the cell cycle analysis of SK-N-SH cells at 48 hr after 1 μM topotecan treatment under serum starvation and 10% FBS by staining the DNA with the propidium iodide (PI) fluorescent dye. Topotecan treatment significantly increased the numbers of SK-N-SH cells in the S and G2/M phases under 10% FBS (Figures 4B, S5A, and S5B, Histogram of cell cycle analysis, related Figure 4). However, the increase was significantly suppressed under serum starvation (Figures 4C, S5C, and S5D, Histogram of cell cycle analysis, related Figure 4). Moreover, the number of SK-N-SH cells in the G0/G1 phase was higher under serum starvation than that under 10% FBS. These data collectively suggest that both decreased DNA damage and increased DNA repair activity can facilitate the progression of SK-N-SH cells through the S and G2/M phases due to successful DNA repair and replication, which increases the cell population re-entering the G0/G1 phase, supporting the prediction from our network model.

Topotecan resistance-associated cholesterol-mediated drug efflux

The network model also suggested that the intracellular concentration of topotecan could be decreased in serum-starved SK-N-SH cells via increased topotecan efflux, contributing to topotecan resistance under conditions of serum starvation. To test this prediction, we measured the amount of topotecan inside SK-N-SH cells at 5 min, 24 hr, and 48 hr after treatment with 1 μM topotecan (Figure 5A) by quantitating topotecan in the protein-free supernatant of cell lysates using MRM analysis with RPLC-triple quadrupole mass spectrometry. The amount of topotecan in the cells peaked 5 min after topotecan treatment under both serum starvation and 10% FBS; thereafter, it gradually decreased. Importantly, the amount of topotecan

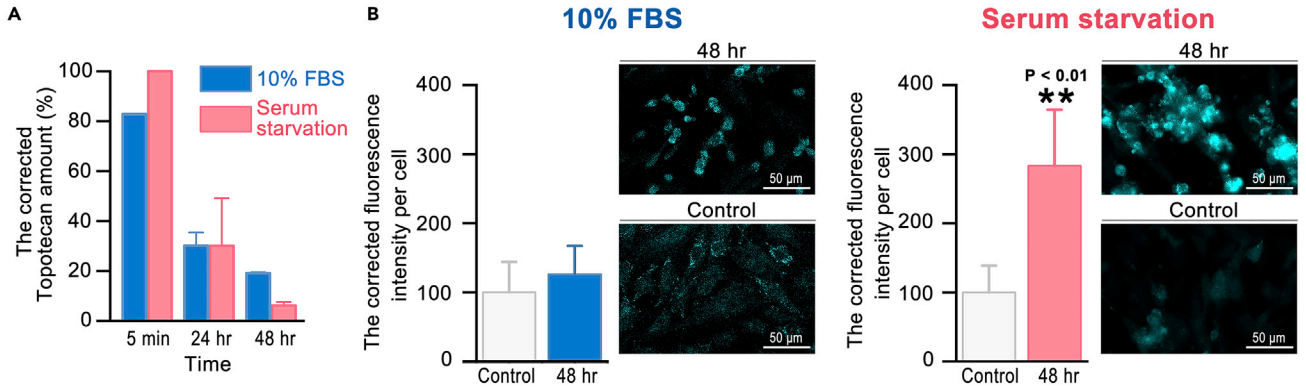

Figure 5. Quantitative analysis of cellular topotecan and membrane cholesterol Bar plots present the level of cellular topotecan ±S.D values (n = 3) (A) Fluorescence bar plot and imaging of filipin III-stained membrane cholesterol for SK-N-SH cells (B). The bar plots present mean ± S.E. values (n = 3). **p < 0.01.

was significantly (33%) lower under serum starvation than that under 10% FBS, 48 hr after topotecan treatment. This observation suggests that either the metabolism or efflux of topotecan was increased at 48 hr. Previously, the metabolism of topotecan was shown to reach a maximum level after 15 min in the isolated perfused rat liver (Platzer et al., 1998). Although the abundances of CYP enzymes responsible for topotecan metabolism can differ between serum-starved neuroblastoma cells and rat liver cells, topotecan seems to be rapidly metabolized following treatment. Considering the upregulation of the proteins involved in the cholesterol-mediated topotecan efflux at 48 hr, the decreased amount of topotecan is more likely due to the increased efflux of topotecan. Notably, the survival rate of serum-starved SK-N-SH cells started to significantly ($p < 0.01$) increase 48 hr after treatment (Figure 1A).

To correlate the cellular amount of topotecan with cholesterol-mediated topotecan efflux, we measured the amount of cholesterol located in the membrane of SK-N-SH cells at 48 hr after exposure to topotecan via cholesterol assay using filipin III, a histochemical stain for cholesterol that emits fluorescence at wavelengths ranging from 385 to 470 nm (Drabikowski et al., 1973). The representative fluorescence images of the fixed SK-N-SH cells revealed that the amount of cholesterol was significantly ($p < 0.01$) higher on the surface of the cells under serum starvation than that under 10% FBS (Figure 5B). Together with the upregulation of DHCR24 confirmed by western blotting (Figure 3E), these data suggest that more cholesterol was synthesized and effluxed under serum starvation conditions in topotecan-treated SK-N-SH cells, consistent with the prediction from the network model. The network model suggested that the whole cholesterol synthesis pathway was upregulated based on the upregulation of metabolic enzymes involved in the pathway. Metabolomic analysis of serum-starved SK-N-SH cells can be employed to further confirm whether the abundance of the intermediate metabolites was increased under conditions of serum starvation.

Topotecan resistance-associated alterations in cell cycle distribution and cholesterol efflux

We showed the dose-dependent topotecan resistance in human neuroblastoma cells (SK-N-SH, SH-SY5Y, and SK-N-BE) under conditions of serum starvation (Figure 1). The aforementioned experiments supported the validity of topotecan resistance factors (i.e., increased DNA repair and cholesterol-mediated topotecan efflux) predicted from the network model in serum-starved SK-N-SH cells. To examine the general validity of these resistance factors in nutrient-deprived neuroblastoma cells, we next performed the same analyses in SH-SY5Y and SK-N-BE cells (Figure 6). The western blots showed that 1 μM topotecan upregulated the expression of both BLM and DHCR24 proteins under conditions of serum starvation in SH-SY5Y cells but only upregulated DHCR24 in SK-N-BE cells (Figures 6A and 6B).

Upon culturing SH-SY5Y and SK-N-BE cells in the presence of 10% FBS, the levels of activated caspase-3/7 released into the culture media increased to 112 and 111%, respectively, 48 hr after treatment with 1 μM topotecan (Figure S6, Bar-plots depicting the levels of activated caspase-3/7 at 48 hr and 72 hr in SH-SY5Y and SK-N-BE cells, related Figure 6). This increasing pattern was more evident 72 hr after treatment with 1 μM topotecan. These results are consistent with the findings in SK-N-SH cells. In contrast, serum-starved SH-SY5Y and SK-N-BE cells exhibited significantly ($p < 0.01$) lower DNA damage than those under

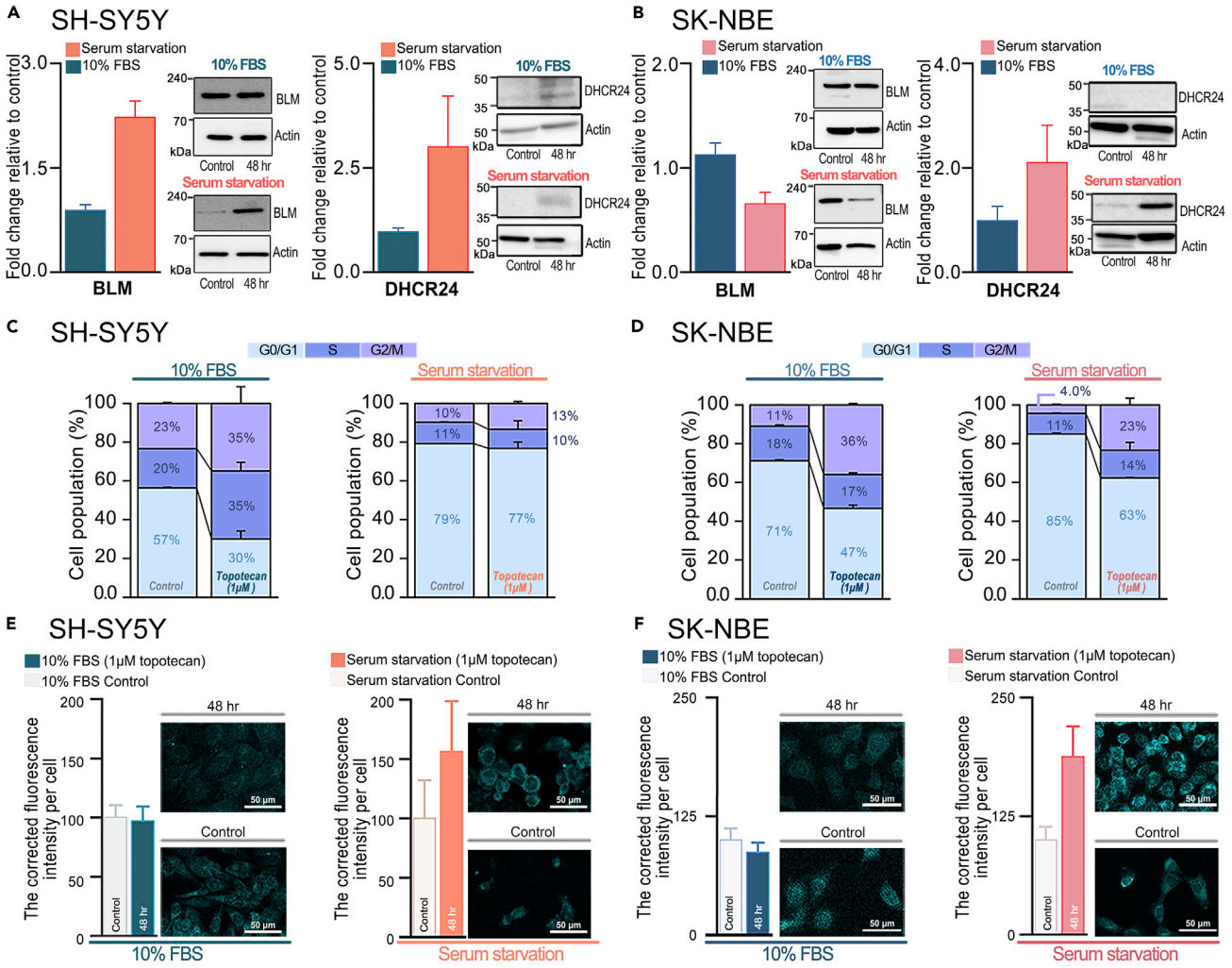

Figure 6. IB quantification, Cell cycle analysis, and membrane cholesterol quantification in SH-SY5Y and SK-N-BE

IB quantification of BLM and DHCR24 (48 hr vs. control) of SH-SY5Y (A) and SK-N-BE (B). The bar plots present mean ± S.D. values (n = 3). Cell cycle analysis of propidium iodide stained SH-SY5Y (C) and SK-N-BE (D) cells. Fluorescence bar plot and image of filipin III-stained membrane cholesterol for SH-SY5Y (E) and SK-N-BE (F) cells. Data are expressed as mean ± S.D. values (n = 3). Fluorescence data are expressed as mean ± S.E. derived from three independent experiments (n = 3).

10% FBS, as indicated by the decreased levels of activated caspase-3/7, particularly 72 hr after 1 μM topotecan treatment (88.7 and 96.7% in SH-SY5Y and SK-N-BE cells, respectively). The finding that there was relatively more DNA damage in SK-N-BE cells than that in SK-N-SH and SH-SY5Y cells was in agreement with the observation that there was no apparent increase in DNA repair activity (i.e., BLM protein levels) in SK-N-BE cells (Figure 6A), unlike the increased DNA repair activity in the other two cell types. This also correlated with the relatively lower topotecan resistance (i.e., less increased viability) of SK-N-BE cells (Figure 1).

Cell cycle analysis further showed that the numbers of both SH-SY5Y and SK-N-BE cells in the S and G2/M phases after 1 μM topotecan treatment decreased under serum starvation compared to that under 10% FBS, similar to SK-N-SH cells (Figures 6C, 6D, and S7, Cell cycle analysis in SH-SY5Y and SK-N-BE, related Figure 6). These data suggest that the decreased DNA damage and/or the increased DNA repair facilitated cell cycle progression through the S and G2/M phases in serum-starved SH-SY5Y and SK-N-BE cells similar to that in serum-starved SK-N-SH cells, thereby increasing the cell population re-entering the G0/G1 phase. Interestingly, the cell cycle shift associated with topotecan resistance

was less apparent in serum-starved SK-N-BE cells. This is consistent with no apparent upregulation of BLM and less reduction of DNA damage, resulting in less effective facilitation of the cell cycle progression compared to that in serum-starved SK-N-SH and SH-SY5Y cells. Moreover, the membrane cholesterol levels were increased in serum-starved SH-SY5Y and SK-N-BE cells after treatment with 1 μM topotecan than that in the cells cultured with 10% FBS (Figures 6D and 6E). This finding was consistent with the upregulation of DHCR24 observed in the two cell types, similar to that in the serum-starved SK-N-SH cells.

In summary, these results indicate that topotecan resistance was induced in serum-starved SK-N-SH and SH-SY5Y cells via increased DNA repair and cholesterol-mediated topotecan efflux. However, in serum-starved SK-N-BE cells, the resistance was predominantly induced by increased cholesterol-topotecan efflux. SH-SY5Y is a third subclone cell line derived from SK-N-SH that demonstrates neuronal function and differentiation (Biedler et al., 1973). Nevertheless, SH-SY5Y cells still share topotecan resistance factors with their parent SK-N-SH cells under nutrient-deprived conditions. Therefore, our study demonstrated the resistance factors, increased DNA repair and/or cholesterol-mediated topotecan efflux applicable to topotecan resistance in all three neuroblastoma cells used in this study and possibly to topotecan resistant tumor cells of the patients.

DISCUSSION

We investigated the dose-dependent effects of the anticancer drug topotecan on SK-N-SH, SH-SY5Y, and SK-N-BE human neuroblastoma cells under serum starvation. Given the difficulty of controlling the tumor burden and substantial toxicity after chemotherapy, it is necessary to develop an effective strategy to improve treatment regimens with higher drug efficacy and fewer adverse effects. To address these issues for topotecan, we studied its pharmacodynamics to understand the mechanism underlying the resistance to a high concentration of topotecan (1 μM) observed in serum-starved SK-N-SH cells. Quantitative proteomic analysis and functional enrichment analysis indicated that DNA damage was decreased, and DNA repair mediated by the ATR-CHK1 pathway was increased in the serum-starved cells to promote survival. Network analysis further suggested that high topotecan concentrations triggered cholesterol-mediated efflux in the cells under serum starvation, contributing to topotecan resistance. DNA damage assay and analyses of the cell cycle and cholesterol in the neuroblastoma cells supported the validity of these resistance factors. Finally, we demonstrated that cholesterol-mediated resistance was generally applicable and DNA repair further accelerated this resistance.

Previously, several mechanisms underlying the development of topotecan resistance have been elucidated using topotecan resistant cells generated via continuous exposure to topotecan (Rasheed and Rubin, 2003). These mechanisms can be categorized into the following: (1) altered accumulation and transport of topotecan, involving reduced accumulation of topotecan due to impaired energy-dependent uptake (Ma et al., 1998) and increased efflux of topotecan via overexpression of ABCB1 (Klejewski et al., 2017) and ABCG2 (Ricci et al., 2016; Yang et al., 2000), (2) mutations of TOP1—such as R364H mutation near the catalytic tyrosine (Urasaki et al., 2001) and E418K mutation (Chang et al., 2002)—that affect the formation of topotecan-stabilized TOP1-DNA complex (irreversible TOP1cc), and (3) altered downstream responses to the formation of the irreversible TOP1cc, including increased DNA repair via overexpression of XRCC1 (Park et al., 2002). These mechanisms can differ from those induced by alterations in tumor microenvironment including nutrient deprivation investigated in this study. The increase in DNA repair could be a shared mechanism in the two resistance models generated by continuous exposure and serum starvation. However, the specific upregulated DNA repair pathways were different in the two resistance models (i.e., ATR-CHK1 DNA repair pathway under serum starvation, and XRCC1-mediated DNA excision repair pathway after continuous exposure to topotecan). Similarly, the efflux of topotecan could be increased in both the resistance models; however, cholesterol-mediated topotecan efflux was increased under serum starvation while ABCB1 or ABCG2-mediated topotecan efflux was upregulated after continuous exposure. Interestingly, serum starvation resulted in the coordinated activation of multiple resistance mechanisms, such as DNA repair and cholesterol-mediated topotecan efflux, thereby leading to reduced DNA damage. However, this coordinated activation of multiple mechanisms was not manifested in the continuous exposure model, probably because the selection of topotecan-resistant cells by continuous exposure ended whenever one of the resistance factors was activated. In contrast, serum starvation can alter multiple cellular pathways to effectively induce the development of resistance against topotecan. Therefore, our

results indicate that topotecan resistance should be tested in diverse tumor microenvironments to define a more complete list of resistance factors.

To test the clinical relevance of these resistance factors, it should be evaluated whether alterations in these factors (e.g., upregulation of BLM and DHCR24 representing increased DNA repair and cholesterol-mediated topotecan efflux, respectively) correlate with topotecan resistance in a large cohort of patients with topotecan-sensitive and resistant neuroblastoma. In clinical settings, the alterations in validated resistance factors in a large cohort can be then evaluated in tumor cells from patients prior to topotecan treatment. For example, the abundance of BLM and DHCR24 could be evaluated using immunohistochemistry during histological examinations or by western blotting in primary tumor cells established from tumor tissues. Evaluating whether the abundance of the markers exceeds the threshold values identified in large cohorts can enable the prediction of the therapeutic outcomes of topotecan treatment for individual patients. For patients who are predicted to be resistant to topotecan, alternative therapeutics or options can be recommended, thereby improving the therapeutic strategy for high-risk neuroblastoma.

In this study, we identified upregulated cholesterol synthesis and trafficking that could increase the topotecan efflux using proteomic analysis of serum-starved neuroblastoma cells. However, it is possible that metabolic pathways other than cholesterol synthesis were dysregulated under conditions of serum starvation. For example, the levels of metabolites related to cholesterol, such as sphingolipids and phospholipids, or reactive oxygen species could be altered under serum starvation conditions. Therefore, metabolomic analysis of serum-starved SK-N-SH cells can be employed to identify other altered metabolic pathways that are associated with the development of topotecan resistance. Finally, our approach of integrating pharmacodynamics, proteomics, and network analysis—possibly together with metabolomic analysis—can be employed for diverse chemotherapeutic drugs toward which high-risk cancers show dose-dependent resistance for characterizing the resistance factors and thereby optimizing the therapeutic strategies.

Limitations of the study

Our research discovered the cellular factors (increased DNA repair and cholesterol-mediated topotecan efflux) for topotecan resistance and the mechanistic links of these factors to topotecan resistance in serum-starved neuroblastoma cells that reflect the characteristics of tumor cells located in the deeper region of solid tumors. However, to test the clinical relevance of these findings, it should examined be whether alterations (e.g., upregulation of BLM and DHCR24) correlate with topotecan resistance in a large cohort of patients with topotecan-sensitive and resistant neuroblastoma.

Resource availability

Lead contact

Further information and requests for resources and reagents should be directed to and will be fulfilled by the lead contact, Hugh I. Kim (hughkim@korea.ac.kr).

Materials availability

This study did not generate new unique reagents.

Data and code availability

The accession number for the the mass spectrometry proteomics data reported in this paper is ProteomeXchange Consortium: PXD014648 via the PRIDE (Perez-Riverol et al., 2019) partner repository.

METHODS

All methods can be found in the accompanying Transparent methods supplemental file.

SUPPLEMENTAL INFORMATION

Supplemental information can be found online at https://doi.org/10.1016/j.isci.2021.102325.

ACKNOWLEDGMENTS

This work was supported by the Korea Basic Science Institute (KBSI) National Research Facilities & Equipment Center (NFEC) grant funded by the Korea government (Ministry of Education) (2019R1A6C1010028 and 2020R1A6C103A027) and the Collaborative Genome Program for Fostering New Post-Genome Industry (NRF-2017M3C9A5031597) of the National Research Foundation of Korea (NRF), funded by the Ministry of Science, ICT, and Future Planning. This work was also supported by the NRF of Korea (2019R1A2C2086193), the National Research Council of Science and Technology of Korea (CRC-15-04-KIST), and the Korea University Future Research Grant. We acknowledge the KBSI for confocal measurements. H.I.K thanks Prof. Min-Sik Kim at Daegu Gyeongbuk Institute of Science & Technology (DGIST) for the critical discussion of the manuscript.

AUTHOR CONTRIBUTIONS

S.Y.C., D.N., A.H., D.I., J.H., C.K., and S.K. conducted the experiments. S.Y.C., A.H., H.I.K., S.-W.L., and D.H. designed the experiments. S.Y.C., D.Y. H., A.H., T.D.L., and D.N. analyzed the data. S.Y.C., D.Y. H., D.N., A.H., J.W.L., H.I.K., S.-W.L., and D.H. wrote the paper.

DECLARATION OF INTERESTS

The authors declare no competing financial interests.

Received: September 21, 2020
Revised: February 16, 2021
Accepted: March 15, 2021
Published: April 23, 2021

REFERENCES

Adamson, B., Smogorzewska, A., Sigoillot, F.D., King, R.W., and Elledge, S.J. (2012). A genome-wide homologous recombination screen identifies the RNA-binding protein RBMX as a component of the DNA-damage response. Nat. Cell Biol. *14*, 318–328.

Alcindor, T., and Beauger, N. (2011). Oxaliplatin: a review in the era of molecularly targeted therapy. Curr. Oncol. *18*, 18–25.

Van Arendonk, K.J., and Chung, D.H. (2019). Neuroblastoma: tumor biology and its implications for staging and treatment. Children *6*, 12.

Biedler, J.L., Helson, L., and Spengler, B.A. (1973). Morphology and growth, tumorigenicity, and cytogenetics of human neuroblastoma cells in continuous culture. Cancer Res. *33*, 2643–2652.

Chang, J.Y., Liu, J.F., Juang, S.H., Liu, T.W., and Chen, L.T. (2002). Novel mutation of topoisomerase I in rendering cells resistant to camptothecin. Cancer Res. *62*, 3716–3721.

Cheung, N.K., and Dyer, M.A. (2013). Neuroblastoma: developmental biology, cancer genomics and immunotherapy. Nat. Rev. Cancer *13*, 397–411.

Cohn, S.L.P., Andrew, A.D., London, W.B., Monclair, T., Ambros, P.F., Brodeur, G.M., Faldum, A., Hero, B., Iehara, T., Machin, D., et al. (2009). The international neuroblastoma risk group (INRG) classification system: an INRG task force report. J. Clin. Oncol. *27*, 289–297.

Coldman, A.J., Fryer, C.J.H., Elwood, J.M., and Sonley, M.J. (1980). Neuroblastoma: influence of age at diagnosis, stage, tumor site, and sex on prognosis. Cancer *46*, 1896–1901.

De Ioris, M., Castellano, A., Ilari, I., Garganese, M., Natali, G., Inserra, A., De Vito, R., Ravà, L., De Pasquale, M.D., Locatelli, F., et al. (2011). Short topotecan-based induction regimen in newly diagnosed high-risk neuroblastoma. Eur. J. Cancer *47*, 572–578.

Drabikowski, W., Łagwińska, E., and Sarzała, M.G. (1973). Filipin as a fluorescent probe for the location of cholesterol in the membranes of fragmented sarcoplasmic reticulum. Biochim. Biophys. Acta *291*, 61–70.

Edmondson, R., Broglie, J.J., Adcock, A.F., and Yang, L. (2014). Three-dimensional cell culture systems and their applications in drug discovery and cell-based biosensors. Assay Drug Dev. Technol. *12*, 207–218.

Gottesman, M.M. (2002). Mechanisms of cancer drug resistance. Ann. Rev. Med. *53*, 615–627.

Gregg, R.W., Molepo, J.M., Monpetit, V.J., Mikael, N.Z., Redmond, D., Gadia, M., and Stewart, D.J. (1992). Cisplatin neurotoxicity: the relationship between dosage, time, and platinum concentration in neurologic tissues, and morphologic evidence of toxicity. J. Clin. Oncol. *10*, 795–803.

Halakos, E.G., Connell, A.J., Glazewski, L., Wei, S., and Mason, R.W. (2019). Bottom up proteomics reveals novel differentiation proteins in neuroblastoma cells treated with 13-cis retinoic acid. J. Proteomics *209*, 103491.

Herd, F., Basta, N.O., McNally, R.J.Q., and Tweddle, D.A. (2019). A systematic review of re-induction chemotherapy for children with relapsed high-risk neuroblastoma. Eur. J. Cancer *111*, 50–58.

Hiyama, E., and Hiyama, K. (2005). Molecular and biological heterogeneity in neuroblastoma. Curr. Genomics *6*, 319–332.

Holohan, C., Van Schaeybroeck, S., Longley, D.B., and Johnston, P.G. (2013). Cancer drug resistance: an evolving paradigm. Nat. Rev. Cancer *13*, 714.

Höckel, M., and Vaupel, P. (2001). Tumor hypoxia: definitions and current clinical, biologic, and molecular aspects. JNCI *93*, 266–276.

Huang, D.W., Sherman, B.T., and Lempicki, R.A. (2008). Bioinformatics enrichment tools: paths toward the comprehensive functional analysis of large gene lists. Nucleic Acids Res. *37*, 1–13.

Johnsen, J.I., Dyberg, C., Fransson, S., and Wickström, M. (2018). Molecular mechanisms and therapeutic targets in neuroblastoma. Pharmacol. Res. *131*, 164–176.

Johnsen, J.I., Dyberg, C., and Wickström, M. (2019). Neuroblastoma—a neural crest derived embryonal malignancy. Front. Mol. Neurosci. *12*, 9.

Khaitan, D., Chandna, S., B Arya, M., and Dwarakanath, B. (2006). Establishment and characterization of multicellular spheroids from a human glioma cell line; Implications for tumor therapy. J. Translat. Med. *4*, 12.

Kim, J.B. (2005). Three-dimensional tissue culture models in cancer biology. Sem. Cancer Biol. *15*, 365–377.

Klejewski, A., Świerczewska, M., Zaorska, K., Brązert, M., Nowicki, M., Zabel, M., and Januchowski, R. (2017). New and old genes associated with topotecan resistance

development in ovarian cancer cell lines. Anticancer Res. *37*, 1625–1636.

Koivusalo, R., and Hietanen, S. (2004). The cytotoxicity of chemotherapy drugs varies in cervical cancer cells depending on the p53 status. Cancer Biol. Ther. *3*, 1177–1183.

Kollmannsberger, C., Mross, K., Jakob, A., Kanz, L., and Bokemeyer, C. (1999). Topotecan – a novel topoisomerase I inhibitor: pharmacology and clinical experience. Oncology *56*, 1–12.

Lambert, S., Mizuno, K.i., Blaisonneau, J., Martineau, S., Chanet, R., Fréon, K., Murray, J.M., Carr, A.M., and Baldacci, G. (2010). Homologous recombination restarts blocked replication forks at the expense of genome rearrangements by template exchange. Mol. Cell *39*, 346–359.

Leclair, M.-D., Hartmann, O., Heloury, Y., Fourcade, L., Laprie, A., Mechinaud, F., Munzer, C., and Rubie, H. (2004). Localized pelvic neuroblastoma: excellent survival and low morbidity with tailored therapy—the 10-year experience of the French society of pediatric oncology. J. Clin. Oncol. *22*, 1689–1695.

Lee, H., Mun, D.-G., So, J.E., Bae, J., Kim, H., Masselon, C., and Lee, S.-W. (2016). Efficient exploitation of separation space in two-dimensional liquid chromatography system for comprehensive and efficient proteomic analyses. Anal. Chem. *88*, 11734–11741.

Levin, V.A., Panchabhai, S.C., Shen, L., Kornblau, S.M., Qiu, Y., and Baggerly, K.A. (2010). Different changes in protein and phosphoprotein levels result from serum starvation of high-grade glioma and adenocarcinoma cell lines. J. Proteome Res. *9*, 179–191.

Li, Y., He, B., Hu, L., Huang, X., Yun, Z., Liu, R., Zhou, Q., and Jiang, G. (2018). Characterization of mercury-binding proteins in human neuroblastoma SK-N-SH cells with immobilized metal affinity chromatography. Talanta *178*, 811–817.

Liscovitch, M., and Lavie, Y. (2000). Multidrug resistance: a role for cholesterol efflux pathways? Trends Biochem. Sci. *25*, 530–534.

Longley, D., and Johnston, P. (2005). Molecular mechanisms of drug resistance. J..Pathol. *205*, 275–292.

Ma, J., Maliepaard, M., Nooter, K., Loos, W.J., Kolker, H.J., Verweij, J., Stoter, G., and Schellens, J.H. (1998). Reduced cellular accumulation of topotecan: a novel mechanism of resistance in a human ovarian cancer cell line. Br. J. Cancer *77*, 1645–1652.

Macaire, P., Morawska, K., Vincent, J., Quipourt, V., Marilier, S., Ghiringhelli, F., Bengrine-Lefevre, L., and Schmitt, A. (2019). Therapeutic drug monitoring as a tool to optimize 5-FU-based chemotherapy in gastrointestinal cancer patients older than 75 years. Eur. J. Cancer *111*, 116–125.

Maeda, H., and Khatami, M. (2018). Analyses of repeated failures in cancer therapy for solid tumors: poor tumor-selective drug delivery, low therapeutic efficacy and unsustainable costs. Clin. Translat. Med. *7*, 7–11.

Maris, J.M. (2010). Recent advances in neuroblastoma. NJEM *362*, 2202–2211.

Maris, J.M., and Matthay, K.K. (1999). Molecular biology of neuroblastoma. J. Clin. Oncol. *17*, 2264.

Maris, J.M., Hogarty, M.D., Bagatell, R., and Cohn, S.L. (2007). Neuroblastoma. Lancet *369*, 2106–2120.

Minchinton, A.I., and Tannock, I.F. (2006). Drug penetration in solid tumours. Nat. Rev. Cancer *6*, 583–592.

Morgenstern, D.A., Baruchel, S., and Irwin, M.S. (2013). Current and future strategies for relapsed neuroblastoma: challenges on the road to precision therapy. J. Pediatr. Hematol. Oncol. *35*, 337–347.

Mossé, Y.P., Deyell, R.J., Berthold, F., Nagakawara, A., Ambros, P.F., Monclair, T., Cohn, S.L., Pearson, A.D., London, W.B., Matthay, K.K., et al. (2014). Neuroblastoma in older children, adolescents and young adults: a report from the International Neuroblastoma Risk Group project. Pediatr. Blood Cancer *61*, 627–635.

Ngan, E.S.-W. (2015). Heterogeneity of neuroblastoma. Oncoscience *2*, 837–838.

Niu, N., and Wang, L. (2015). In vitro human cell line models to predict clinical response to anticancer drugs. Pharmacogenomics *16*, 273–285.

Park, S.Y., Lam, W., and Cheng, Y.C. (2002). X-ray repair cross-complementing gene I protein plays an important role in camptothecin resistance. Cancer Res. *62*, 459–465.

Park, J.-M., Park, J.-H., Mun, D.-G., Bae, J., Jung, J.H., Back, S., Lee, H., Kim, H., Jung, H.-J., Kim, H.K., et al. (2015). Integrated analysis of global proteome, phosphoproteome, and glycoproteome enables complementary interpretation of disease-related protein networks. Sci. Rep. *5*, 18189.

Park, J.R., Stewart, C.F., London, W.B., Santana, V.M., Shaw, P.J., Cohn, S.L., and Matthay, K.K. (2006). A topotecan-containing induction regimen for treatment of high risk neuroblastoma. J. Clin. Oncol. *24*, 9013.

Platzer, P., Schaden, S., Thalhammer, T., Hamilton, G., Rosenberg, B., Silgoner, I., and Jäger, W. (1998). Biotransformation of topotecan in the isolated perfused rat liver: identification of three novel metabolites. Anticancer. Res. *18*, 2695–2700.

Pommier, Y. (2006). Topoisomerase I inhibitors: camptothecins and beyond. Nat. Rev. Cancer *6*, 789–802.

Rasheed, Z.A., and Rubin, E.H. (2003). Mechanisms of resistance to topoisomerase I-targeting drugs. Oncogene *22*, 7296–7304.

Ricci, J.W., Lovato, D.M., Severns, V., Sklar, L.A., and Larson, R.S. (2016). Novel ABCG2 antagonists reverse topotecan-mediated chemotherapeutic resistance in ovarian carcinoma xenografts. Mol. Cancer Therap. *15*, 2853.

Rodríguez-Hernández, A., Brea-Calvo, G., Fernández-Ayala, D.J., Cordero, M., Navas, P., and Sánchez-Alcázar, J.A. (2006). Nuclear caspase-3 and caspase-7 activation, and poly(ADP-ribose) polymerase cleavage are early events in camptothecin-induced apoptosis. Apoptosis *11*, 131–139.

Scaturro, P., Stukalov, A., Haas, D.A., Cortese, M., Draganova, K., Płaszczyca, A., Bartenschlager, R., Götz, M., and Pichlmair, A. (2018). An orthogonal proteomic survey uncovers novel Zika virus host factors. Nature *561*, 253–257.

Starobova, H., and Vetter, I. (2017). Pathophysiology of chemotherapy-induced peripheral neuropathy. Front. Mol. Neurosci. *10*, 174.

Stiller, C.A., and Parkin, D.M. (1992). International variations in the incidence of neuroblastoma. Int. J. Cancer *52*, 538–543.

Urasaki, Y., Laco, G.S., Pourquier, P., Takebayashi, Y., Kohlhagen, G., Gioffre, C., Zhang, H., Chatterjee, D., Pantazis, P., Pommier, Y., et al. (2001). Characterization of a novel topoisomerase I mutation from a camptothecin-resistant human prostate cancer cell line. Cancer Res. *61*, 1964.

Yang, C.H., Schneider, E., Kuo, M.L., Volk, E.L., Rocchi, E., and Chen, Y.C. (2000). BCRP/MXR/ABCP expression in topotecan-resistant human breast carcinoma cells. Biochem. Pharmacol. *60*, 831–837.

Zanoni, M., Piccinini, F., Arienti, C., Zamagni, A., Santi, S., Polico, R., Bevilacqua, A., and Tesei, A. (2016). 3D tumor spheroid models for in vitro therapeutic screening: a systematic approach to enhance the biological relevance of data obtained. Sci. Rep. *6*, 19103.

iScience, Volume *24*

Supplemental information

DNA repair and cholesterol-mediated drug efflux induce dose-dependent chemoresistance in nutrient-deprived neuroblastoma cells

Soo Yeon Chae, Dowoon Nam, Do Young Hyeon, Areum Hong, Timothy Dain Lee, Sujin Kim, Dongjoon Im, Jiwon Hong, Chaewon Kang, Ji Won Lee, Daehee Hwang, Sang-Won Lee, and Hugh I. Kim

Table of Contents

Contents

1. TRANSPARENT METHODS

Experimental model and subject details. SK-N-SH neuroblastoma cells were purchased from the Korea Cell Line Bank (Seoul, Korea) and were also generously provided by the Samsung Medical Center (Seoul, Korea). SH-SY5Y neuroblastoma cells were purchased from the Korea Cell Line Bank (Seoul, Korea). SK-N-BE cells were generously provided by the Samsung Medical Center. The cells were cultured in a 1:1 mixture of Dulbecco's modified Eagle's medium/F-12 Nutrient Mixture Ham (DMEM/F-12; WelGENE, Daegu, Korea) supplemented with 10% FBS (Capricorn Scientific GmbH, Ebsdorfergrund, Germany) and 1% antibiotics (10,000 U/mL penicillin G, 10,000 μg/mL streptomycin, and 25 μg/mL amphotericin B; Hyclone, Logan, UT, USA). The antibiotics were sterilized prior to use by passage through a 0.2 μm filter. The cells were cultured by incubating at 37 °C in a humidified atmosphere containing 5% CO_2. The serum-starved SK-N-SH cells were cultured in the absence of FBS for 24 hr prior to treatment with topotecan.

Cell viability assay. Cells were cultured in DMEM/F12 containing both 10% FBS and 1% antibiotics or 1% antibiotics for serum starvation experiments. Cells (1.5×10^4) were seeded in each well of a 96-well plate and incubated for 24 h. The seeded cells were treated with 0, 0.1, 1, 5, and 10 nM and 0.1, 1, and 10 μM of topotecan prepared in 0.1% dimethyl sulfoxide (DMSO; Junsei, Tokyo, Japan). Cell viability assays were performed 0, 24, 48, and 72 hr after topotecan treatment using the CCK-8 kit (Dojindo Molecular Technologies, Inc., Kumamoto, Japan), and absorbance was measured at 450 nm. The cell viability at each dose was tested in triplicate, and the assay was repeated three times to confirm reproducibility (Tominaga et al., 1999).

Protein Extraction and Digestion. The cells were lysed in lysis buffer (4% SDS, 0.1 M Tris-HCl pH 7.6) using a probe sonicator (Q55 Sonicator, Qsonica; repeating 30 s on ice, 5 times). The homogenate was centrifuged at 16,000 *g* at 20 °C for 10 min and the supernatant was transferred to a new tube. Protein concentration was measured using the BCA protein assay (BCA Protein Assay Kit, Pierce). The lysates obtained from 12 different cell suspensions were individually digested using the filter aided sample preparation (FASP) protocol (Wisniewski et al., 2009). The proteins were reduced in SDT buffer (4% sodium dodecyl sulfate [SDS] in 0.1 M Tris-HCl, pH 7.6, and 0.1 M dithiothreitol [DTT]) at 37 ºC for 45 min with shaking at 300 rpm and were denatured for 10 min at 95 ºC using a Comfort thermomixer (Eppendorf, Hamburg, Germany). The protein samples were then transferred to a YM-30 membrane filter (Millipore Corporation, Billerica, MA, USA)-Aldrich and mixed with 200 μL of 8 M urea prepared in 0.1 M Tris-HCl (pH 8.5). The protein samples in the membrane filters were centrifuged three times at 14,000 ×*g* and 20 ºC for 60 min to remove SDS. Subsequently, 100 μL of 0.05 M iodoacetamide was mixed with 8 M urea and incubated for 25 min at 20–22 ºC in the dark to alkylate the free thiol groups in the proteins. The protein samples in the membrane filters were then diluted with 200 μL of 8 M urea and concentrated four times. Finally, 100 μL of 50 mM ammonium bicarbonate (pH 8.0) was added, and the samples were centrifuged at 14,000 ×*g* and 20 ºC for 30 min (twice). Trypsin (Promega, Madison, WI, USA) was added to the filter unit at an enzyme-to-protein ratio of 1:50 (w/w), and the proteins were digested overnight at 37 ºC. Second digestion was performed using trypsin (1:100 ratio) at 37 ºC for 6 h. The resulting peptides were eluted by centrifugation at 14,000 ×*g* and 20 ºC for 30 min. The filter was rinsed with 60 μL of 50 mM ammonium bicarbonate and was centrifuged at 14,000 ×*g* and 20 ºC for 20 min. The peptides in the eluents were combined, dried, and stored at −80 ºC until subsequent TMT labeling.

TMT labeling of peptides. As shown in Figure 2A and S3A, each set of the six peptide samples obtained from the 0.1 and 1 μM topotecan treatment groups was respectively labeled with a 6-plex TMT reagent (Thermo Fisher Scientific, Waltham, MA, USA). For each channel of the 6-plex TMT, 100 μg of peptides was labeled according to the manufacturer's instructions (Thermo Fisher Scientific). The peptide sample was mixed with the TMT reagent, vortexed briefly, and incubated for 1 hr at 20 ºC in a thermomixer. The excess reagents were quenched by the addition of 8 μL of 5% hydroxylamine (Sigma-Aldrich) and subsequent incubation for 20 min at 20 ºC. Each set of TMT-labeled peptide samples was pooled and dried using vacuum centrifugation.

Phosphopeptide Enrichment. For extensive phosphopeptide enrichment, we performed "one-pot" immobilized metal affinity chromatography (IMAC), modified from a previously described method (Mun et al.,

2019). Briefly, for each set of the 0.1 and 1 μM topotecan treatment groups, 250 μL of Ni-NTA magnetic beads (1 mL, 36111, Qiagen) were washed three times with deionized water (DIW). Then, the beads were treated with 200 μL of EDTA and 200 μL of 10 mM aqueous $FeCl_3$ in a step by step manner. With each step, magnetic beads were incubated for 30 min on an end-to-end rotator and washed three times with 200 μL of DIW. Before adding the peptide samples, the beads were washed with 800 μL of washing buffer (20% water with 0.1 % TFA in acetonitrile). The TMT-labeled peptides were resuspended in 1 mL of washing buffer and added to the magnetic beads. The solution was incubated for 30 min on an end-to-end rotator and the supernatant (i.e. flow-through sample from IMAC) was collected for the global proteomic profiling experiment. Beads were gently washed 4 times with 1 mL of washing buffer, and each supernatant was collected as a global peptide. After removing the non-phosphopeptide from the beads, 250 μL of the elution buffer (1:1 acetonitrile/2.5% ammonia in 2 mM phosphate buffer, pH 10) was added to the beads, following which, they were vortexed every 30 s for 1.5 min. The suspension was transferred to a new tube and acidified with 10% TFA to obtain pH in the range of 3.5–4. Finally, 2 sets of phosphopeptides were vacuum dried and desalted using a C18 spin column while the flow-through peptides were vacuum dried and stored at -80 ºC.

Online fractionation using DO-NCFC-RP/RPLC. A previously developed online noncontiguous fractionating and concatenating device coupled with a dual RPLC system was modified to generate 24 NCFC fractions (Lee et al., 2015; Lee et al., 2016). Briefly, online NCFC device consists of mid-pH RP column (150 μm × 50 cm) attached to a function selection valve (6-port/ 3-channel/ 2-position, C72MX-4676, VICI) and two NCFC valves (25-port/ 1-channel/ multi-position, C5M-66024D, VICI) interconnected with 24 NCFC loops (200 μm × 22.3 cm) was employed. Two sets of SPE column (150 μm × 3 cm) and analytical column (75 μm × 100 cm) were installed to two-column valves (6-port/3-channel/2-position, C72MX-4676, VICI). The temperatures of the mid-pH column and analytical column were controlled at 60 ºC (Hyung et al., 2011). Jupiter C18 materials (3 μm, 300 Å, Phenomenex) were used for the in-house manufacturing of mid-pH column, two SPE columns, and two analytical columns (Lee et al., 2012). The system was operated using four binary pumps (two Ultimate 3000 NCP-3200RS and two Ultimate 3000 NCP-3200RS Proflow, Dionex, Thermo Fisher Scientific) and one autosampler (Ultimate 3000 WPS-3000TPL RS, Dionex, Thermo Fisher Scientific).

For both global proteome and phosphoproteome analysis, a mid-pH solvent A (10mM TEAB in water, pH 7.5) and a mid-pH solvent B (10mM TEAB in 99% ACN, pH 7.5) were used for 1st -dimensional separation. In the case of global proteome analysis, 50 μg of labeled peptides were injected and separated using gradient consisting of 1–50% mid solvent B with a 1 μL/min flow rate for 120 min. At the same time, two NCFC valves were synchronously rotated with a 1-minute interval for 5 cycles so that the eluates from the mid-pH RP column were subsequently collected into NCFC loops. Therefore, 5 noncontiguous eluates were deposited into each of the 24 NCFC loops and prepared for 2nd-dimensional separation. For phosphoproteome analysis, the same 120 min gradient with 0.5 μL/min flow rate was used to obtain 12 NCFC fractions. In order to collect 12 NCFC fractions, two NCFC valves were used to perform two-step rotations (e.g., 1 → 3 → 5 → … → 23 → 1).

For 2nd dimensional separation, each of NCFC fractions derived from both global proteome and phosphoproteome analysis were acidified and diluted 10 times with dilution buffer (0.2% TFA in water) while transferring to the SPE column. For global proteome analysis, a 120-minute gradient method was used for analytical column separation with the following gradient of solvent A (0.1% formic acid in water) and solvent B (0.1% formic acid in ACN): from 10 to 40% solvent B over 107 min, from 40 to 80% solvent B over 5 min, 80% solvent B for 8 min at a flow rate of 0.3 μL/min. For phosphoproteome analysis, a 180-minute gradient method was used with identical solvent A and solvent B as follows: from 10 to 40% solvent B over 167 min, from 40 to 80% solvent B over 5 min, 80% solvent B for 8 min at a flow rate of 0.3 μL/min.

Mass spectrometry analysis. Both global proteome and phosphoproteome analyses were performed using quadrupole-orbitrap mass spectrometry (Exploris 480, Thermo Fisher Scientific) with high-field asymmetric waveform ion mobility spectrometry (FAIMS Pro™ Interface, Thermo Fisher Scientific) at the Center of Proteogenome Research. The peptides eluted from the analytical column were ionized using an in-house

nano-electrospray equipped with dual emitters manufactured by the chemical etching of a fused-silica capillary (Kelly et al., 2007). MS was performed in the positive electrospray ionization (ESI) mode with an electric potential of 3 kV. The temperature of the desolvation capillary was set at 250 ºC, and the temperature of both inner and outer electrodes of FAIMS were set at 100 ºC. Nitrogen was used as the FAIMS carrier gas that was turned on for 1 min at the end of each experiment. Voltages of -35V, -50V, and -65V were considered as multiple compensation voltages (CV) of FAMIS with a cycle time of 1 s. For each CV, full MS scans ranging from 350 to 1400 Th were acquired at a resolution of 60,000 and a maximum ion injection time of 20 ms. The monoisotopic precursor selection (MIPS) mode was activated for peptides and those with a minimum intensity of 100000 were filtered. The isolation window of 1.2 Th were fragmented using a data-dependent acquisition method with normalized collision energy (NCE) of 28 for higher-energy collisional dissociation (HCD). The MS/MS scans were obtained at a resolution of 15,000 with a fixed first mass of 120 Th and a maximum ion injection time of 32 ms. The exclusion duration was set to 25 s, and the charge states of 2-5 and undetermined ions were included. The normalized automatic gain control (AGC) target values of full MS and MS/MS scans were set to 500 and 1,000, respectively.

Database search for peptide identification. The precursor masses of the MS/MS scans were refined using Multiplexed Post-Experiment Monoisotopic Mass Refinement (mPE-MMR) prior to conducting the database search (Madar et al., 2017). The MS/MS data (e.g., mgf files) were searched against a protein database consisting of the UniProt human reference database (released June 2018, including 94,744 entries) and common contaminants (179 entries) using the MS-GF+ search engine (v9949, http://proteomics.ucsd.edu/software-tools/ms-gf/). For global proteome datasets, database searches were performed with the following parameters: semi-tryptic cleavage and a precursor mass tolerance of 10 ppm. For static modifications, TMT (+229.162932 Da) on lysine and N-terminus and carbamidomethylation (+57.0214 Da) on cysteine were considered. Methionine oxidation (+15.994915 Da) along with asparagine and glutamine deamidation were set as variable modifications. For phosphoproteome datasets, phosphorylation of serine, threonine, and tyrosine were used as additional variable modifications. The search results were filtered using a false discovery rate of 1% peptide spectrum match (PSM)-level, which was estimated using the target decoy search strategy. From the global proteome data of 0.1 and 1 μM topotecan-treated cells, we identified 285,027 and 281,156 non-redundant peptides that included 58,273 and 61,882 semi-tryptic peptides, respectively. From the phosphoproteome data of 0.1 and 1 μM topotecan-treated cells, we identified 42,241 and 61,151 non-redundant phosphopeptides that included 6,148 and 8,088 semi-tryptic peptides, respectively.

The MS proteomics data have been deposited in the ProteomeXchange Consortium via the PRIDE partner repository, with the dataset identifier PXD014648.

Identification of DEPs and differentially expressed phosphopeptides. To identify differentially expressed peptides, we first selected unique peptides with a precursor ion purity ≥ 70% as the peptides with reliable quantification-based TMT intensities. For each of these selected peptides, we computed the $\log_2$-fold-change in TMT intensity between 48 hr and the control under 0.1 μM and 1 μM starvation, and 0.1 μM and 1 μM FBS conditions. The intensities of TMT 127 and 131 were used to compare the $\log_2$-fold-changes in cells incubated with 10% FBS, while the intensities of TMT 126 and 130 were used for serum-starved cells. Next, we identified the differentially expressed peptides as the ones with absolute $\log_2$-fold-changes > 1 (2-fold). Of the proteins with differentially expressed peptides as sibling peptides, we identified the differentially expressed proteins (DEPs) as the ones with two or more differentially expressed peptides in the same direction of regulation (up- or down-). Proteins with two or more differentially expressed peptides in both directions of the regulation (both up- and down-) were excluded. Although the DEPs were identified in the 5 min post topotecan treatment vs. control data, these were not analyzed since drug resistance was not observed at 5 min and the DEPs were mostly associated with stress responses to drug treatment. The differentially expressed phosphopeptides were identified in the same way with the differentially expressed peptides.

Protein extraction and immunoblotting. The cells were seeded in serum starvation media or 10% FBS media for 24 h. Control cells were harvested within 1 min of treatment with 0.1% DMSO and topotecan-treated cells were harvested after 48 hr of treatment. Total protein lysates were prepared by lysing cells in RIPA buffer containing phosphatase inhibitor and protease inhibitor, followed by centrifugation at 7500 $\times g$

for 5 min. Bradford and bicinchoninic acid protein assay kits (Thermo Fisher Scientific) were used to determine the protein concentration in whole lysates. A total of 25–50 µg of each cell lysate was loaded on 8% and 12% gels for SDS-PAGE and transferred to a polyvinylidene fluoride membrane (Bio-Rad Laboratories, Inc., California, USA). The following antibodies were used at a dilution of 1:1000: rabbit anti-24-dehydrocholesterol reductase (DHCR24) antibody (Invitrogen, Carlsbad, USA), mouse anti-DHCR24 (Santa Cruz in., California, USA), mouse anti-BLM (1:1000) (Invitrogen), mouse anti-BLM (Abcam Cambridge UK), and β-actin (Invitrogen). After probing with the appropriate species-specific horseradish peroxidase (HRP)-linked secondary antibodies (1:10000), the proteins were detected using EZ-Western and EZ-Western Lumi Femto kits (DoGenBio, Seoul, Korea) and a LAS mini 4000 (GE Healthcare, Amersham, UK). Data were analyzed using the ImageJ software (NIH, Bethesda. MD, USA).

Quantitative analysis of topotecan uptake. SK-N-SH cells were seeded on cell culture dishes (SPL Life Science, Seoul, Korea) in serum starvation or 10% FBS media for 24 hr and then treated with 1 µM topotecan. After 5 min, 24 hr, and 48 hr, the cells were washed with phosphate-buffered saline (PBS; Hyclone) and detached from the cell culture dish using 0.25% trypsin. The cells were resuspended in water, lysed using the freeze-thaw method and osmotic lysis, and centrifuged at 14,000 $\times g$ and 4 °C for 15 min. The supernatants were used to quantify cellular topotecan uptake in the following manner. The proteins were precipitated by mixing with ACN (J. T. Bakers, Phillipsburg, NJ, USA) at a 1:1 ratio for 10 min and then removed by centrifugation at 7,500 $\times g$ and 4°C for 5 min. The protein-free supernatants were purified by fractionation using an SPE cartridge (Waters). The sample solutions were lyophilized, and the solid samples were reconstituted with a mobile phase and analyzed using RPLC-TQMS to quantitate the amount of topotecan. The number of cells was normalized to the protein concentration measured using the Bradford assay by dividing the MRM intensity of topotecan by the amount of cellular protein proportional to the number of cells. Cellular topotecan uptake after every 24 hr correlated with cell viability observed from 24 to 48 hr after drug treatment. Therefore, we quantified the amount of topotecan in serum-starved SK-N-SH cells for up to 48 hr after treatment with 1 µM topotecan every 24 hr. The initial cellular topotecan uptake amount was measured 5 min after drug treatment.

Time-resolved MRM analysis was performed using TQMS with a model LCMS-8050 spectrometer (Shimadzu, Kyoto, Japan) in both positive and negative ion modes. The source parameters were 300 (interface), 250 (DL), and 400 ºC (heating gas temperatures). The nebulizing, heating, and drying gases had a flow rate of 3, 10, and 10 L/min, respectively. An ACQUITY BEH C_{18} 1.7 µm VANGUARD Pre-Co (Waters) and a Shimadzu-pack C_{18} 3 µm (Shimadzu) were used for LC separation at 40 ºC. The injection volume of the sample solution was 10 µL. Water (J. T. Baker) containing 0.1% formic acid (Tokyo Chemical Industry Co., Tokyo, Japan) (A) and 0.1% formic acid ACN (B) were used as solvents at a flow rate of 0.1 mL/min. The LC time program was scheduled as follows: 0-10 min, 0% B; 10-40 min; the concentration of B increased linearly from 0 to 95%; 40-50 min; 95% B; 50-60 min; sharp reduction to 0% B. m/z = 422.00 represented the protonated topotecan ion that fragmented to m/z = 377.05, 46.10, and 320.00.

DNA damage assay. Cells were cultured in DMEM/F12 containing both 10% FBS and 1% antibiotics or 1% antibiotics for serum starvation experiments. Cells (1.5×10^4) were seeded in each well of a 96-well plate (15,000 cell/well) and incubated for 24 hr. The seeded cells were treated with 0, 0.1, and 1 µM topotecan prepared in 0.1% DMSO. DNA damage assays were performed at 0, 24, 48, and 72 hr after topotecan treatment using the CellEvent Caspase-3/7 green detection reagent (Thermo Fisher Scientific). The excitation/emission of the samples was analyzed at 502/530 nm.

Cell cycle analysis. SK-N-SH, SH-SY5Y, and SK-N-BE cells were seeded in culture dishes (SPL Life Science) at a density of 2.7×10^6 cells/mL in serum starvation or 10% FBS media for 24 hr. Next, the cells were treated with 0.1% DMSO for 1 min (control samples) or with 1 µM topotecan for 48 hr (48 hr samples). The cells were washed with PBS and detached from the culture dish using 0.25% trypsin. For fixation and permeabilization, the cells were fixed with ice-cold 70% ethanol at 4 ºC for 30 min and centrifuged; the supernatant was then decanted. FxCycle™ PI/RNase staining solution (Thermo Fisher Scientific; 0.5 mL) was added to 1.0×10^6 cells for DNA staining. The PI-stained cells were analyzed by fluorescence-activated cell sorting using an Accuri C6 Plus device (BD, San Jose, CA, USA).

Filipin III staining. Filipin III was prepared at a concentration of 1 mg/mL in DMSO (stock solution) and stored at –20 ºC. For preparing the working solution, filipin III was diluted to 0.25 mg/mL using 10% FBS-PBS; this solution was used for staining the membrane cholesterol. SK-N-SH, SHY-SY5Y, and SK-N-BE cells were seeded in confocal dishes (SPL Life Science) at a density of 6.7×10^4 cells/mL in 10% FBS or serum starvation medium at 37°C in a humidified atmosphere containing 5% CO_2. After 24 hr, the cells were treated with 0.1% DMSO for 1 min (control samples) or 1 μM topotecan for 48 hr (48 hr samples). To avoid cytotoxicity resulting from filipin III staining, the cells were fixed with ice-cold 4% paraformaldehyde prepared in PBS for 2 hr at 20 ºC and treated with 2.5 mg/mL glycine to quench paraformalin. Paraformaldehyde and glycine were obtained from Tokyo Chemical Industry Co. The cells were stained with filipin (working solution) for 2 hr at 20 ºC, and fluorescence was observed using a confocal microscope (IMP-LSM or LSM 780 NLO; Carl-Zeiss, Baden-Wurttembergm, Germany) and an Axio Observer D1 fluorescence inverted microscope (Carl-Zeiss). The samples were excited at 405 nm for confocal microscopy, and a 4′,6-diamidino-2-phenylindole filter was used for inverted fluorescence microscopy. The images were analyzed using the ImageJ software (NIH).

Quantification and statistical analysis. All details regarding the number of cells, experimental replicates, and the level of significance are described in the figure and captions. Significance of comparisons is indicated in figures and supplemental data as $*p < 0.05$, and $**p < 0.01$

2. Supplemental Data Items

Table S1. Table depicting the viability of human neuroblastoma cells, related Figure 1. Table depicting the viability of SK-N-SH, SK-N-BE, and SH-SY5Y cells in the presence of various concentrations of topotecan. Data are expressed as mean and ± SE from three independent experiments.

A. SK-N-SH

Serum starvation

Time (hr)	0.1 nM	1 nM	5 nM	10 nM	0.1 µM	1 µM	10 µM
0	97.91 ± 2.45	98.33 ± 2.62	101.27 ± 4.02	102.12 ± 0.92	97.42 ± 1.32	105.44 ± 0.97	116.54 ± 0.98
24	120.1 ± 9.5	112.27 ± 9.82	114.32 ± 8.52	120.24 ± 13.54	116.24 ± 9.43	123.77 ± 6.88	93.76 ± 2.55
48	112.75 ± 1.31	109.02 ± 1.04	118.49 ± 1.97	119.93 ± 2.00	114.65 ± 7.08	**155.04 ± 6.04	107 ± 2.97
72	126.54 ± 7.8	126.78 ± 6.77	*146.32 ± 13.62	*137.69 ± 8.45	*141.68 ± 7.63	**179.07 ± 12.26	102.84 ± 3.64

Significant differences *p<0.05, **p<0.01

10% FBS

Time (hr)	0.1 nM	1 nM	5 nM	10 nM	0.1 µM	1 µM	10 µM
0	101.08 ± 3.87	97.83 ± 3.56	100.62 ± 3.47	96.41 ± 2.47	98.79 ± 3.09	98.42 ± 2.19	98.96 ± 2.16
24	100.9 ± 1.7	104.83 ± 2.86	99.16 ± 2.5	96.04 ± 2.68	81.33 ± 5.76	**61.96 ± 5.63	**35.62 ± 4.29
48	99.29 ± 1.69	97.9 ± 1.81	94.36 ± 1.96	89.03 ± 2.32	68.34 ± 3.77	**46.91 ± 4.84	**10.33 ± 1.92
72	100.68 ± 3.53	96.95 ± 3.05	93.01 ± 4.42	86.27 ± 5.16	**62.97 ± 5.69	**39.32 ± 4.69	**4.83 ± 1.35

Significant differences *p<0.05, **p<0.01

B. SH-SY5Y

Serum starvation

Time (hr)	0.1 nM	1 nM	5 nM	10 nM	0.1 µM	1 µM	10 µM
0	96.88 ± 3.8	92.25 ± 2.85	90.33 ± 2.95	93.6 ± 3.53	91.78 ± 3.31	99.83 ± 2.41	106.24 ± 3.32
24	89.79 ± 3.19	94.18 ± 3.89	91.34 ± 2.38	90.07 ± 2.05	89.41 ± 4.78	91.91 ± 11.57	*66.99 ± 8.95
48	89.4 ± 6.17	108.48 ± 8.7	107.61 ± 9.23	109.36 ± 17.2	97.59 ± 14.46	109.8 ± 19.37	74.32 ± 16.69
72	88.66 ± 2.07	112.63 ± 6.73	103.59 ± 8.95	100.22 ± 12.34	110.32 ± 13.47	130.64 ± 18.03	84.47 ± 15.45

Significant differences *p<0.05, **p<0.01

10% FBS

Time (hr)	0.1 nM	1 nM	5 nM	10 nM	0.1 µM	1 µM	10 µM
0	103.72 ± 1.87	99.19 ± 2.66	97.58 ± 2.72	98.97 ± 3.14	117.57 ± 6.43	117.54 ± 3.71	111.63 ± 2.28
24	104.17 ± 2.71	115.31 ± 4.11	114.47 ± 4.75	116.49 ± 4.2	85.89 ± 5.87	66.46 ± 4.53	**38.21 ± 2.96
48	97.52 ± 1.94	98.25 ± 3.32	92.78 ± 3.42	91.17 ± 3.76	77.29 ± 4.68	**42.58 ± 1.6	**20.21 ± 1.08
72	99.69 ± 2.08	95.04 ± 2.93	95.29 ± 4.05	84.75 ± 2.56	*66.25 ± 4.34	**36.74 ± 7.18	**15.49 ± 4.59

Significant differences *p<0.05, **p<0.01

C. SK-N-BE

Serum starvation

Time (hr)	0.1 nM	1 nM	5 nM	10 nM	0.1 µM	1 µM	10 µM
0	100.72 ± 4.55	99.73 ± 3.68	101.81 ± 4.19	103.79 ± 4.54	100.69 ± 2.46	100.63 ± 4.77	103.08 ± 1.87
24	95.79 ± 1.93	98.6 ± 2.18	104.95 ± 3.08	102.77 ± 3.26	106.78 ± 2.62	110.27 ± 5.25	79.15 ± 4.75
48	100.06 ± 1.84	110.12 ± 2.72	121.17 ± 2.42	114.61 ± 3.12	107.42 ± 5.18	120.12 ± 12.7	75.9 ± 2.2
72	96.94± 2.56	111.87 ± 3.05	112.77 ± 2.96	112.04 ± 3.14	105.75 ± 5.17	119.71 ± 12.04	79.72 ± 3.78

Statistically significant differences *p<0.05, **p<0.01

10% FBS

Time (hr)	0.1 nM	1 nM	5 nM	10 nM	0.1 µM	1 µM	10 µM
0	104.94 ± 4.82	106.9 ± 5.4	112.88 ± 6.89	112.18 ± 7.36	109.93 ± 6.92	104.48 ± 4.31	97.05 ± 5.92
24	96.06 ± 1.52	98.37 ± 2.12	96.55 ± 2.18	94.97 ± 2.96	*74.90 ± 1.35	**65.53 ± 1.96	**58.57 ± 1.17
48	95.65 ± 1.47	96.64 ± 2.02	95.65 ± 2.63	*87.15 ± 1.5	**65.10 ± 1.08	**50.49 ± 1.01	**41.42 ± 0.79
72	96.94 ± 1.7	98.17 ± 2.01	96.79 ± 2.75	*84.47 ± 0.9	**63.84 ± 0.68	**51.98 ± 1.75	**41.55 ± 0.64

Significant differences *p<0.05, **p<0.01

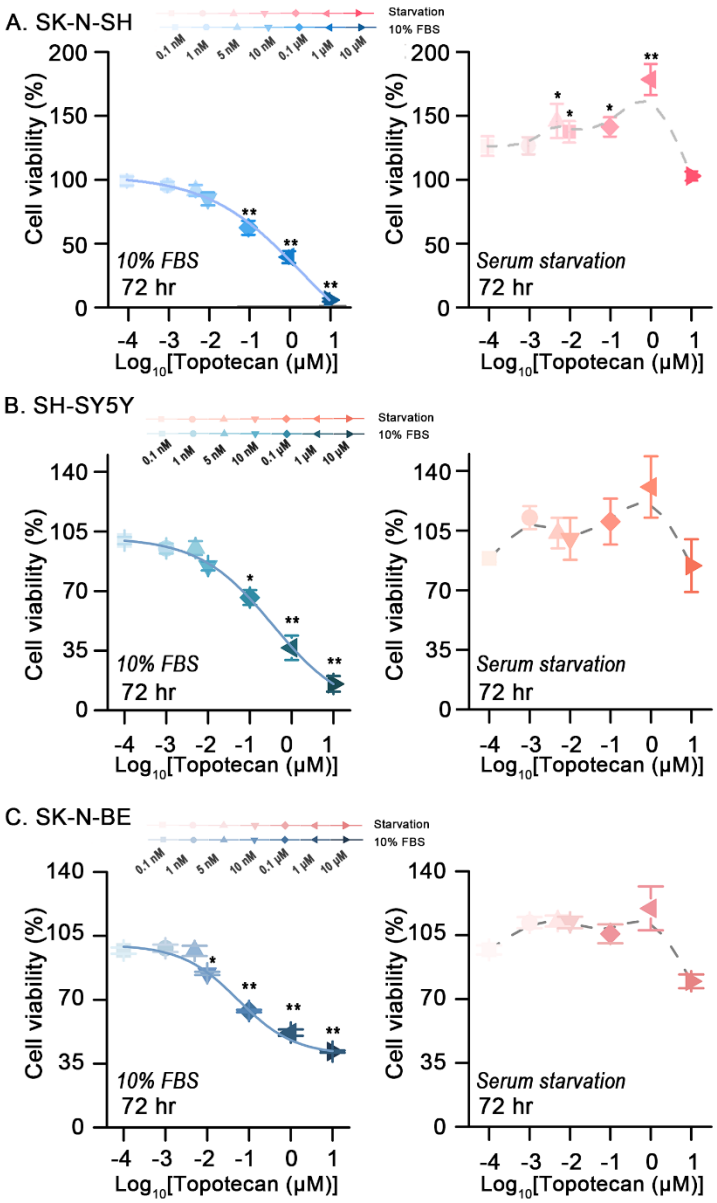

Figure S1. Dose-response viability curves at 72 hr, related Figure 1. Dose-response viability curves of human neuroblastoma cells (SK-N-SH, SH-SY5Y, and SK-N-BE) at 72 hr under conditions of 10% FBS (left) and serum-starvation (right).

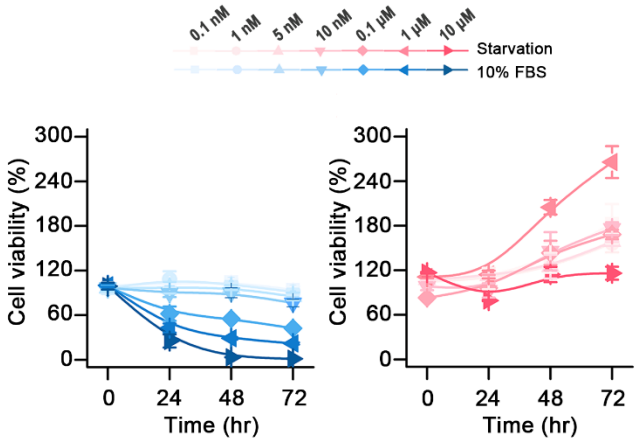

Figure S2. Results of the cell viability assay performed with SK-N-SH cells obtained from a different source (Korea Cell Line Bank), related Figure 1. Results of the cell viability assay performed with SK-N-SH cells obtained from a different source (Korea Cell Line Bank); the cells were exposed to different concentrations of topotecan.

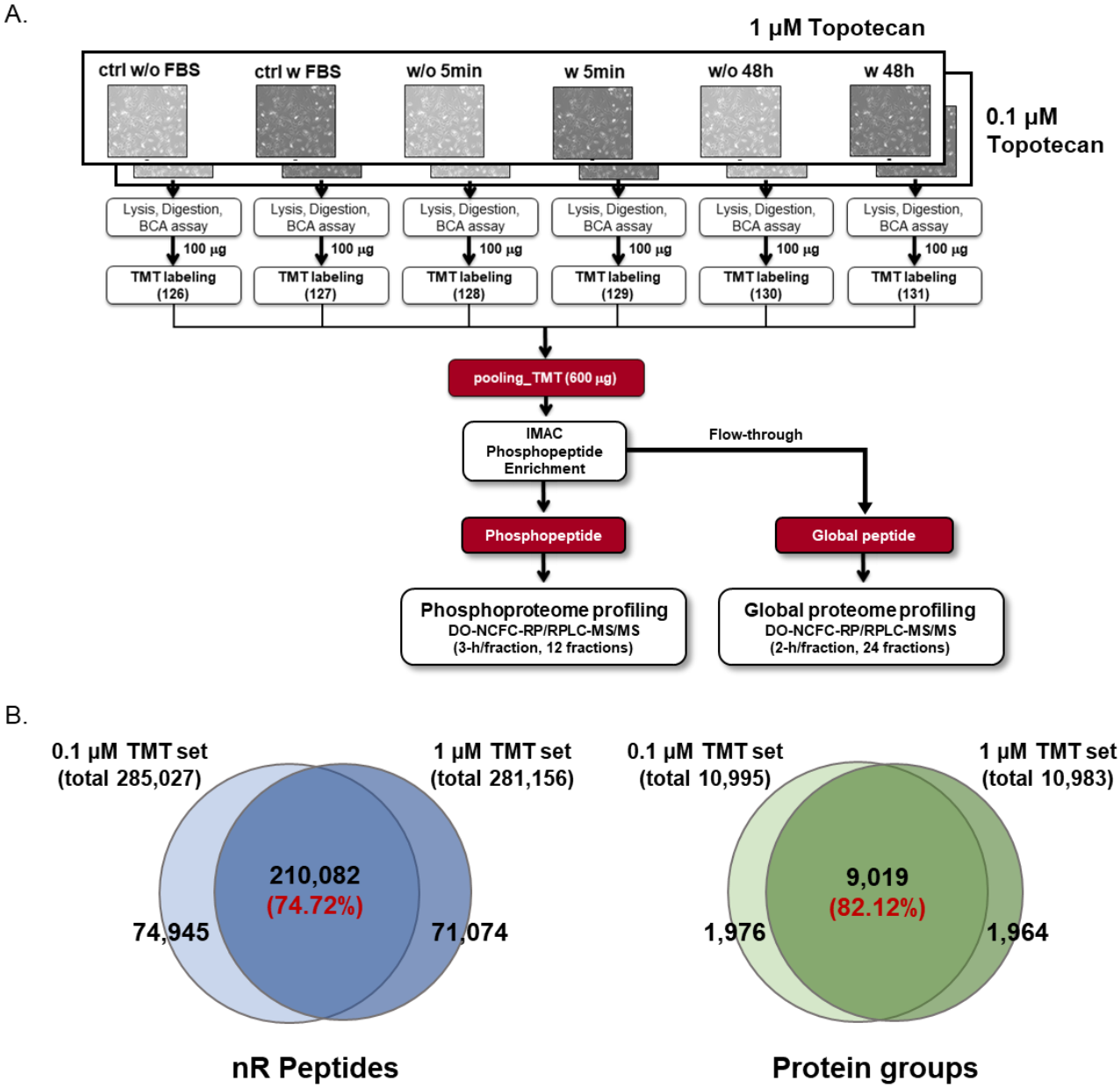

Figure S3. Proteomics experiments, related Figure 2. (A) The overall workflow of proteomics experiments. After treatment with 0.1 and 1 μM of topotecan, two controls, two 5-minute (with and without treatment), and two 48-hour (with and without treatment) peptide samples were labeled with 6-plex TMT. The pooled TMT peptide was subjected to "one-pot" IMAC phosphopeptide enrichment. The enriched phosphopeptide sample was subjected to DO-NCFC-RP/RP-MS/MS experiments with 12 online NCFC fractions and 3-hour LC gradient. The flow-through peptide sample was subjected to DO-NCFC-RP/RP-MS/MS experiments with 24 online NCFC fractions and 2-hour LC gradient. (B) Venn diagram showing the relationships of identified peptides and proteins between the two datasets of TMT experiments.

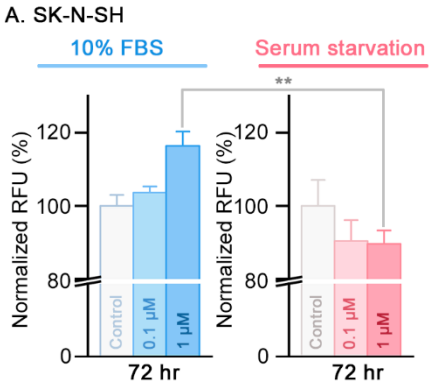

Figure S4. Bar-plot depicting the levels of activated caspase-3/7 at 72 h in SK-N-SH cells, related Figure 4. Plots were generated for cells grown in the presence of 10% FBS and serum-starved SK-N-SH cells. Relative fluorescence units (RFU) were determined under each condition, and the values were normalized by the number of cells in each treatment. Data are represented as mean ± S.D. obtained from three independent experiments.

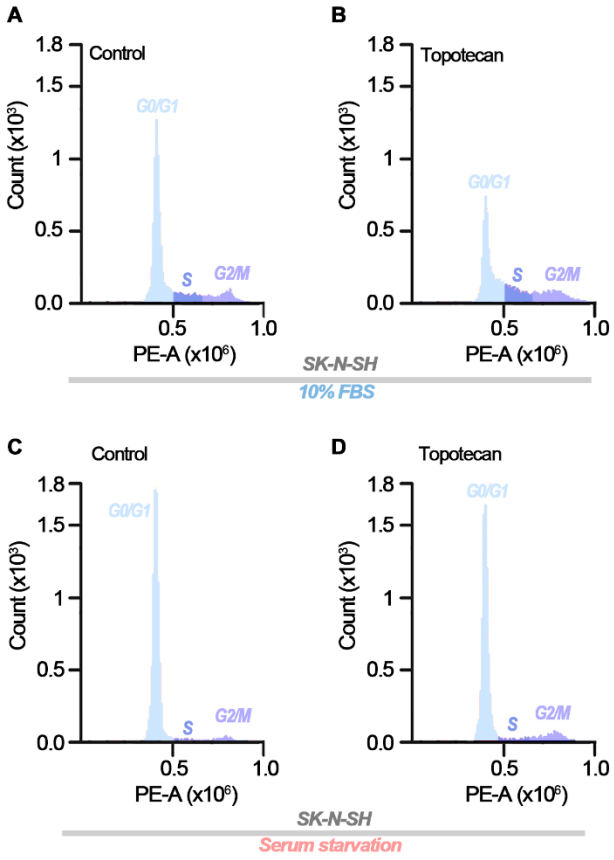

Figure S5. Histogram of cell cycle analysis, related Figure 4. Histogram depicting cell cycle analysis for SK-N-SH cells under conditions of serum starvation (A, B) and 10% FBS (C, D).

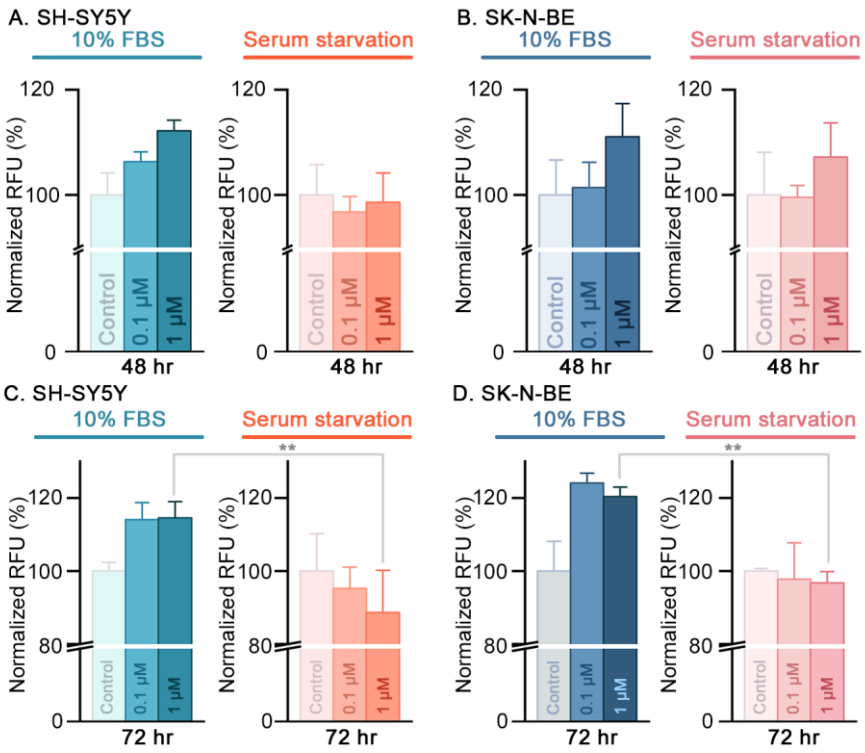

Figure S6. Bar-plots depicting the levels of activated caspase-3/7 at 48 h and 72 h in SH-SY5Y and SK-N-BE cells, related Figure 6. Plots were generated for cells incubated with 10% FBS and serum-starved cells (SH-SY5Y and SK-N-BE cells). Relative fluorescence units (RFU) were determined under each condition, and the values were normalized by the number of cells in each treatment. Data are presented as mean ± S.D. derived from three independent experiments.

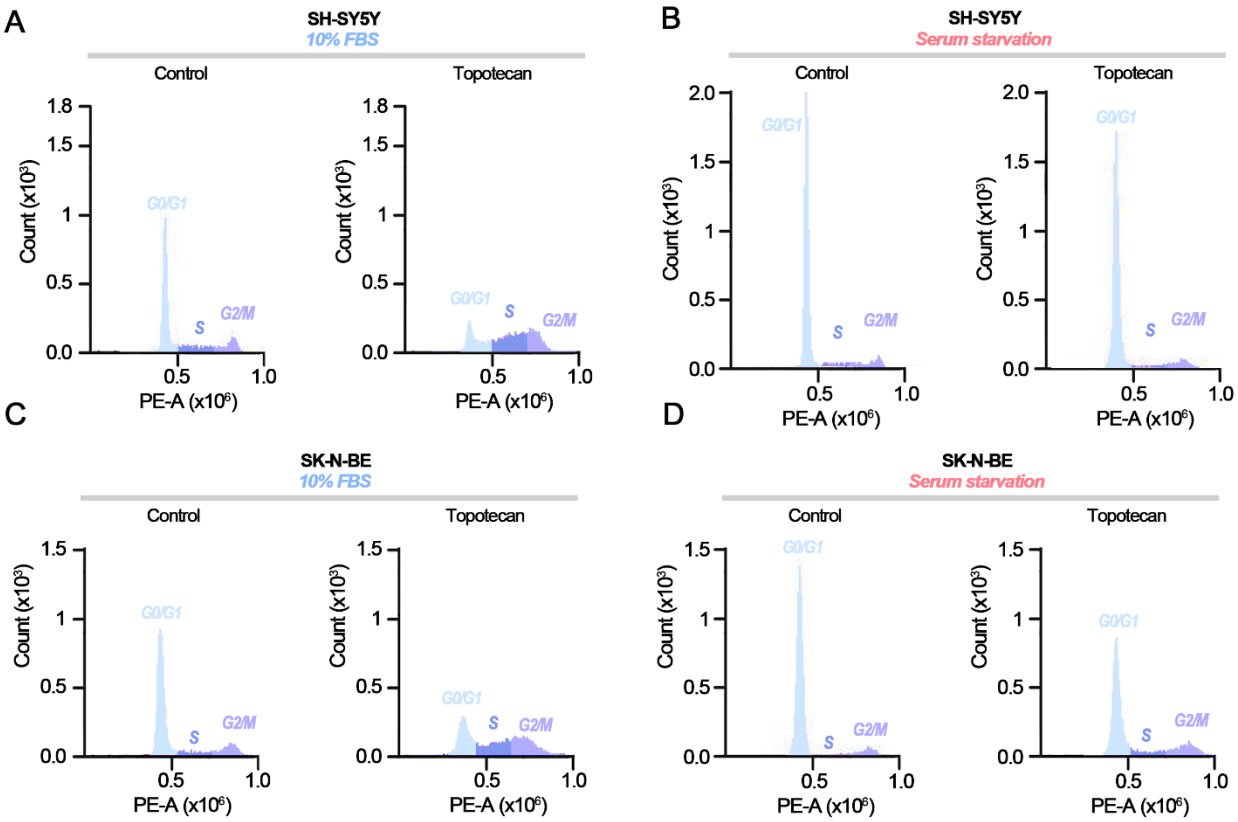

Figure S7. Cell cycle analysis in SH-SY5Y and SK-N-BE, related Figure 6. Histograms depicting cell cycle analysis for SH-SY5Y (A, B) and SK-N-BE (C, D) cells under conditions of 10% FBS (A, C) and serum starvation (B, D).

3. Supplemental References

Tominaga, H., Ishiyama, M., Ohseto, F., Sasamoto, K., Hamamoto, T., Suzuki, K., and Watanabe, M. (1999). A water-soluble tetrazolium salt useful for colorimetric cell viability assay. Anal. Commun. *36*, 47–50.

Wisniewski, J.R., Zougman, A., Nagaraj, N., and Mann, M. (2009). Universal sample preparation method for proteome analysis. Nat. Methods *6*, 359–362.

Mun, D.G.*, et al.* (2019). Proteogenomic characterization of human early-onset gastric cancer. Cancer Cell *35*, 111-124.e110.

Lee, H., Mun, D.-G., Bae, J., Kim, H., Oh, S.Y., Park, Y.S., Lee, J.-H., and Lee, S.-W. (2015). A simple dual online ultra-high pressure liquid chromatography system (sDO-UHPLC) for high throughput proteome analysis. Analyst *140*, 5700–5706.

Lee, H., Mun, D.-G., So, J.E., Bae, J., Kim, H., Masselon, C., and Lee, S.-W. (2016). Efficient exploitation of separation space in two-dimensional liquid chromatography system for comprehensive and efficient proteomic analyses. Anal. Chem. *88*, 11734–11741.

Hyung, S.-W., Kim, M.-S., Mun, D.-G., Lee, H., and Lee, S.-W. (2011). The effect and potential of using a temperature controlled separation column with ultra-high pressure microcapillary liquid chromatography/tandem mass spectrometry on proteomic analysis. Analyst *136*, 2100–2105.

Lee, J.H.*, et al.* (2012). Fully automated multifunctional ultrahigh pressure liquid chromatography system for advanced proteome analyses. Journal of proteome research *11*, 4373–4381.

Kelly, R.T., Page, J.S., Tang, K., and Smith, R.D. (2007). Array of chemically etched fused-silica emitters for improving the sensitivity and quantitation of electrospray ionization mass spectrometry. Anal. Chem. *79*, 4192–4198.

Madar, I.H., Ko, S.-I., Kim, H., Mun, D.-G., Kim, S., Smith, R.D., and Lee, S.-W. (2017). Multiplexed post-experimental monoisotopic mass refinement (mpe-mmr) to increase sensitivity and accuracy in peptide identifications from tandem mass spectra of cofragmentation. Anal. Chem. *89*, 1244–1253.